

Comparing observed and modelled decomposition of the Atlantic Meridional Overturning Circulation at 26°N

MSc Thesis

Author: Jordi Beunk

Student number: 5999448

Email: j.d.beunk@students.uu.nl

1st supervisors: Wilco Hazeleger and Sybren Drijfhout

2nd supervisor: Appy Sluijs

MSc Marine Sciences
Department of Geosciences
Utrecht University



Universiteit Utrecht

Abstract

The Atlantic Meridional Overturning Circulation (AMOC) is the Atlantic part of the global overturning circulation. The role of the AMOC in heat and carbon fluxes impacts the climate system on both a regional and global scale. Our understanding of the strength, variability and structure of the AMOC has improved since the deployment of the RAPID array, which monitors the volume transport at 26°N since April 2004. Additionally, these observations serve as invaluable reference data for the representation of the AMOC in coupled Earth System models. The most recent phase of the Coupled Model Intercomparison Project, CMIP Phase 6, allows us to assess the representation of the AMOC in novel climate models. However, a large inter-model spread combined with disagreement between RAPID data and CMIP6 models suggests that the drivers of the strength and variability of the AMOC are poorly understood. To gain more insight into this disagreement, we decompose the AMOC into several transport components and assess how well the strength, variability and deep-water circulation is reproduced by CMIP6 models. Additionally, we examine future changes in the transport components under SSP585 and relate these changes to the historical mean state.

We show that the underestimation of the historical AMOC strength is likely related to the reduced transport of lower NADW, due to the small scale of Greenland-Iceland-Scotland Ridge overflow compared to the resolution of models and excessive mixing at this location. This is compensated by increased recirculation in the subtropical gyre and more AABW transport in models. Deep-water circulation in models is dominated by a distinct DWBC with minor interior recirculation compared to observations, which is likely related to model resolution. We show that the low-frequency variability of Florida Straits transport is largely overestimated and hypothesize that the inclusion of the Antilles Current in this component in models is a significant contributor to this discrepancy. The variability of NADW is underestimated, most likely due to the inability of models to reproduce lower NADW overflow.

We find that the future decline in the AMOC is dominated by decreased Florida Straits transport, either due to reduced input from the South Atlantic or communication of reduced NADW transport by boundary waves. We find significant relationships ($p < 0.01$) between the historical mean state and future changes of the total AMOC, Ekman and AABW transport. However, these relationships are too weak to be used as “emergent constraints”. Additionally, the relationship cannot be explained by sea ice extent or seasonality in this study.

Our results give insight into the potential causes of disagreement in the modelled and observed AMOC. We underline the importance of similar studies at several latitudes to improve our understanding on the leading drivers of AMOC changes and advise to include RAPID measurements of the Antilles Current in Florida Straits transport in these studies.

Table of Contents

1. Introduction.....	1
2. Data	4
2.1 <i>Observational data</i>	4
2.2 <i>CMIP6 model data</i>	4
3. Methods	6
4. Results	10
4.1 Comparing historical model data with observational estimates	10
4.1.1 <i>Timeseries of components</i>	11
4.1.2 <i>Deep-water circulation</i>	12
4.1.3 <i>Total variability of components</i>	14
4.1.4 <i>Decomposition of variability</i>	16
4.2 SSP585 model data.....	19
4.2.1 <i>Overturning stream function</i>	19
4.2.2 <i>Timeseries of components</i>	19
4.2.3 <i>Deep-water circulation</i>	20
4.2.4 <i>Historical mean vs SSP585 future changes</i>	22
5. Discussion	23
5.1 Historical period	23
5.1.1 <i>Strength of components</i>	23
5.1.2 <i>Deep-water circulation</i>	23
5.1.3 <i>Variability of components</i>	24
5.2 SSP585	26
5.2.1 <i>Contribution of components to AMOC decline</i>	26
5.2.2 <i>Historical mean vs SSP585 future changes</i>	28
5.3 Uncertainties	30
5.4 General remarks	31
6. Conclusion	32
Acknowledgements	33
Code availability	33
References.....	34
Appendices	43
Appendix A	43
Appendix B	43
Appendix C.....	44
Appendix D	46

Appendix E.....	47
Appendix F.....	48
Appendix G	49
Appendix H	50

1. Introduction

The Atlantic Meridional Overturning Circulation (AMOC) is the Atlantic part of the global overturning circulation. In the Atlantic Ocean, relatively warm upper-ocean water is transported northward by the Gulf Stream (Joyce and Zhang, 2010). The Gulf Stream is fed by the Florida Current through the Florida Straits and the Antilles Current, located east of the Bahamas (Morey et al., 2017). A significant part of the transport by the Florida Current originates from the South Atlantic, while the Antilles Current predominantly transports water from the North Atlantic Subtropical Gyre (Bryden, 2021). The Gulf Stream partly transports water further northward into the North Atlantic Current and partly recirculates southward in the North Atlantic Subtropical Gyre (Figure 1). During its transport to higher northern latitudes this water loses heat. In the Labrador, Irminger and Nordic seas cold dense deep-water is formed which is transported southward through the Deep Western Boundary Current (DWBC), which partly recirculates northward in the interior of the deep ocean (Bryden, 2021). The net effect is northward transport of warm upper-ocean water and southward transport of cold deep-water (e.g. Ganachaud, 2003; Johnson et al., 2019). Upwelling of southward transported deep-water occurs primarily in the Southern Ocean by strong westerlies around Antarctica, closing the overturning circulation (Marshall and Speer, 2012). The result is a net northward heat transport by the AMOC, with a maximum of 1.3 PW ($1 \text{ PW} = 10^{15} \text{ W}$) around 26°N (Hall and Bryden, 1982). Additionally, the AMOC contributes considerably to carbon uptake and storage in the deep ocean, representing 30% of the total carbon sink in the North Atlantic (Fontela et al., 2016). The role of the AMOC in heat and carbon fluxes impacts the climate system on both a regional and global scale. Examples of its influence are changes in Arctic sea ice (Mahajan et al., 2011), variations in Europe's climate (Jackson et al., 2015) and shifts in the Intertropical Convergence Zone (ITCZ) impacting Asian monsoons (Cheng et al., 2007). Therefore, knowledge about (the drivers of) changes in the strength and variability of the AMOC are crucial.

The spatial structure of the overturning circulation was first conceptualized by Stommel. In his theory on westward intensification of ocean currents (Stommel, 1948), he showed that upper mid-ocean water is transported southward as a result of the wind stress distribution in the North Atlantic. It is compensated by northward flow by a western intensified boundary current, the Gulf Stream. Additionally, he provided the first model on abyssal circulation in the global ocean (Stommel, 1958). Interior deep water is transported northward and upward, thus upwelling occurs uniformly in the global ocean. The upwelling is balanced by deep water formation, envisaged by Stommel to occur in the North Atlantic and Wendell Sea. The source and sink of deep water are connected by southward flowing Deep Western Boundary Currents. Stommel notes that his model on the structure of the overturning circulation is not an accurate and detailed description, but rather a simplified representation of the ocean circulation. Over the past decades, the view of this so called "conveyor-belt" model driven predominantly by deep water formation has been challenged (Lozier, 2010). It has been shown that, instead of buoyancy forcing, wind forcing could be the primary driver of the overturning circulation. Not only due to its impact on upper ocean transport and deep water recirculation by eddies (Dengler, 2004), but also through its key role in upwelling of deep water (Wunsch, 2002). However, the dominance of either wind or buoyancy forcing on the AMOC might largely depend on time scale (Bjostoch, 2008). Additionally, the location of deep water formation in the North Atlantic subpolar gyre has been subject to debate. Pickart and Spall (2007) suggested that deep convection in the Labrador Sea only plays a minor role in the North Atlantic overturning. Recent observations of the Overturning in the Subpolar North Atlantic Program (OSNAP) are in line with this hypothesis, emphasizing the importance of deep convection in the Irminger and Iceland Sea as subpolar contributors to the strength and variability of the AMOC (Lozier et al., 2019).

The RAPID-MOCHA-WBTS (hereafter RAPID) array played an important role in our understanding of the strength, variability and structure of the AMOC (Rayner et al., 2011). This array monitors the AMOC volume transport at 26°N since April 2004 (Frajka-Williams et al., 2021). The choice of location is motivated by the fact that the overturning maximum generally occurs close to 26°N and that the Gulf Stream is bounded by Florida and the Bahamas at this latitude (Bryden et al., 2009). The transport through the cross section is estimated by the decomposition of the AMOC into three components: (1) transport through the Florida Straits based on electromagnetic cable measurements since 1982, (2) Ekman surface transport, generated by the zonal wind stress, calculated using ERA5 wind stress and (3) density driven interior transport estimated from mooring measurements. These moorings compute density profiles at several locations along the cross section (Figure 1). Using the thermal wind balance, meridional velocities are calculated from zonal density gradients. These velocities can be used to obtain transport through the section. A spatially constant correction is added to the velocity field to assure a net meridional transport of zero (McCarthy et al., 2015). The interior transport is decomposed into the following transport components based on depth intervals: thermocline recirculation (0 – 800m), intermediate water (800 – 1100m), upper North Atlantic Deep Water (1100 – 3000m), lower North Atlantic Deep Water (3000 – 5000m) and Antarctic Bottom Water (> 5000m). The measurements by the RAPID array have provided new insights into the strength and variability of the AMOC. An example is the realisation that the AMOC varies significantly on time scales much shorter than annual to millennial, with significant daily to seasonal fluctuations due to changes in wind forcing (Johnson et al., 2019). Additionally, RAPID data proves to be invaluable in climate modelling, providing reference data to improve the representation of the AMOC in coupled Earth System models (Weijer et al., 2020).

The Coupled Model Intercomparison Project (CMIP), organized by the World Climate Research Programme (WCRP), is a comprehensive effort of modelling centres around the world to improve our understanding about past, present and future changes of the climate system (Eyring et al., 2016). Over the years CMIP not only included more models, but also addressed a broader range of scientific problems. This includes questions about the mean state and variability of the AMOC and its drivers in a warming climate (Eyring et al., 2016). The most recent phase, CMIP Phase 6 (CMIP6), allows us to assess the representation of the AMOC in novel climate models. Even though CMIP6 shows improvements compared to previous CMIP generations, model biases related to the AMOC persist (Fox-Kemper et al., 2021). These include a shallow bias of the North Atlantic Deep Water cell (Weijer et al., 2020), too much North Atlantic deep convection in the temporal and spatial domain (Heuzé, 2021), overestimated sensitivity to anthropogenic aerosol forcing (Menary et al., 2020) and an underestimated temperature difference between the upper and lower limb of the AMOC (Roberts et al., 2020). Additionally, CMIP6 models largely underestimate low-frequency variability of the AMOC and show large inter-model differences in their AMOC representation (Weijer et al., 2020). This large inter-model spread, together with disagreement between RAPID data and CMIP6 models, suggests that the drivers of the strength and variability of the AMOC are poorly understood.

The CMIP6 models are used for future projections in a changing climate. In recent years, a new framework is adopted in which pathways of radiative forcing are combined with alternative socio-economic developments (O'Neill et al., 2014). On the upper end of these so called Shared Socioeconomic Pathways (SSPs) is SSP5-8.5 (hereafter SSP585), where fossil-fueled developments produce a radiative forcing of 8.5 W/m² in 2100 (Kriegler et al., 2017). The scenario simulations are driven by greenhouse gas concentration, and include changes in land use and aerosols (O'Neill et al., 2016; Rao et al., 2017). The projections show several climatic changes by the end of the 21st century (2081-2100) compared to the recent past (1995-2014), which include: a globally averaged surface air temperature increase of 2.4 – 4.8 °C (*very likely*), increased globally averaged annual land

precipitation of 0.9 – 12.9% (*likely*) and an ice-free Arctic Ocean in September (*likely*) (Lee et al., 2021). Additionally, the AMOC is projected to weaken through the 21st century under SSP585 (Weijer et al, 2020).

The goal of this study is to gain more insight into the cause of disagreement between CMIP6 models and RAPID data in terms of AMOC strength and variability. In order to do this, we decompose the total modelled AMOC transport at 26°N into the same transport components as measured by the RAPID array: Florida Straits, Ekman, thermocline recirculation, intermediate water, upper North Atlantic Deep Water, lower North Atlantic Deep Water and Antarctic Bottom Water transport. The modelled strength and variability of these components are compared to RAPID estimations for the overlapping historical period (2004-2014). Additionally, we examine the change of these components under SSP585 until 2100 and discuss the deep-water circulation for both the historical and future period. Finally, we compare the future change under SSP585 with the historical mean state of each component.

The objectives of this study are (1) to examine how well CMIP6 models are able to reproduce the strength and variability of the different transport components of the AMOC, as measured by the RAPID array, (2) to find out how CMIP6 models portray deep-water circulation, (3) to analyse which components dominate the future change of the AMOC under SSP585 and (4) to relate these future changes to the historical mean state of the components. Finally, we give an interpretation of mechanisms driving discrepancies between modelled and observed estimates of the AMOC components.

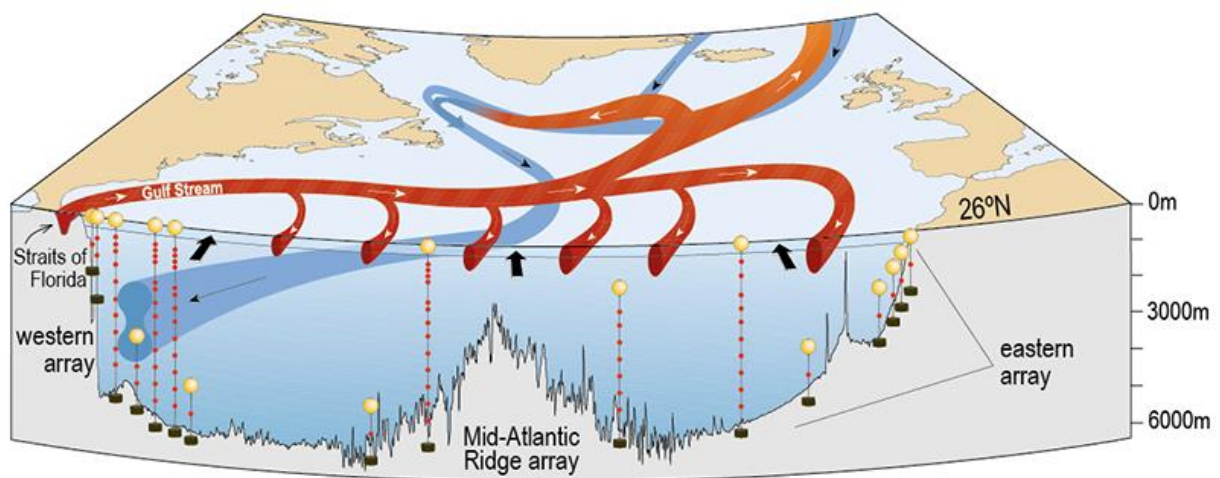


Figure 1: Schematic of the overturning circulation at 26°N. Warm upper-water transport is indicated by red arrows and cold deep-water transport by blue arrow. Black arrows show the dominant direction of Ekman transport. The RAPID moorings are illustrated as well. Figure from Smeed et al. (2014).

2. Data

2.1 Observational data

AMOC estimates of the RAPID array from April 2004 to December 2014 are used in this study (Frajka-Williams et al., 2021). The originally 12-hourly data is monthly averaged to compare it to CMIP6 data. Transport of the total MOC and the different components is analysed, which include: Florida Straits transport (“t_gs10”), Ekman transport (“t_ek10”), thermocline recirculation (“t_therm10”), intermediate water (“t_aiw10”), upper North Atlantic Deep Water (“t_ud10”), lower North Atlantic Deep Water (“t_ld10”) and Antarctic Bottom Water (“t_bw10”). Additionally, we obtained the overturning stream function (“moc_vertical”) from the output data. It is important to note that RAPID data, repeatedly denominated as “observations” in this study, are not direct measurements of transport, but rather indirect estimates. The error in AMOC estimates from RAPID data due to measurement inaccuracies is 0.9 Sv for 10-day averages and 1.5 Sv for annual averages. The error of monthly values used in this study is thus somewhere within this range. A detailed description of the AMOC transport calculation and the estimated accuracy is given in the paper by McCarthy et al. (2015). The RAPID data and notes are available at https://rapid.ac.uk/rapidmoc/rapid_data/datadl.php.

2.2 CMIP6 model data

In this study, historical simulations of 19 CMIP6 models are used. Historical simulations run from 1850 to 2014, but only the period overlapping the RAPID measurements (2004-2014) is analysed. Additionally, the projection under high-end Shared Socioeconomic Pathway 5-8.5 (SSP585) of 18 models is considered for the time period from 2015 to 2100. The choice of these models is motivated by the fact that historical and SSP585 data is available for all used variables. These include the meridional velocity (“vo”), which is the y-ward (i.e. north-south directed) velocity component of the sea water, the zonal wind stress (“tauuo”), which is the stress on the ocean water from the overlying atmosphere due to winds in east-west direction, the salinity (“so”), defined as the salt content of sea water in parts per thousand and the potential temperature (“thetao”), which is the temperature corrected for the pressure effect. Additionally, the overturning stream function (“msftyz”) is obtained of several models that included this variable in the output data. The overturning stream function of all models is also calculated using transport values, as explained in the Method section. Only models that use horizontal depth levels are included, so models with an isopycnic (i.e. density levels) or hybrid ocean are excluded. As model CNRM-ESM2-1 did not include temperature data for the future projection, this model is not included in the analysis of SSP585.

Most models contain multiple ensemble members, which have a specific variant label that indicates the configuration of realisation (r), initialisation (i), physics (p) and forcing (f). For most models, we used the ensemble member with variant label r1i1p1f1. This ensemble member was not available for models CNRM-CM6-1, CNRM-ESM2-1, HadGEM3-GC31-LL, HadGEM3-GC31-MM and UKESM1-0-LL. For these models we used the ensemble member with variant label r1i1p1f2, r2i1p1f2, r1i1p1f3, r1i1p1f3, r1i1p1f2, respectively. Even though the forcing index of these ensemble members varies, the forcing version (v6.2.0) is the same and therefore does not affect our results. The models used in this study are listed in Table 1. The data has been accessed through the Centre for Environmental Data Analysis (CEDA) archive (<https://data.ceda.ac.uk>) and the data intensive supercomputer JASMIN is used for data analysis in Jupyter Notebook. Since approval is needed to access CMIP6 data through the CEDA archive, we added references for open-access data from the Earth System Grid Federation (ESGF) to Table 1.

Table 1: Metadata and references of the models analysed in this study. References are from the Earth System Grid Federation

<i>Model</i>	<i>Modelling centre</i>	<i>Horizontal resolution (°)</i>	<i>Variant label</i>	<i>Data reference historical</i>	<i>Data reference SSP585</i>
CAMS-CSM1-0	CAMS	1 x 1	r11p1f1	Rong (2019)	Rong (2019)
CAS-ESM2-0	CAS	1 x 1	r11p1f1	Chai (2020)	Unknown (2018)
CESM2-WACCM	NCAR	1 x 1	r11p1f1	Danabasoglu (2019)	Danabasoglu (2019)
CIesm	THU	1 x 1	r11p1f1	Huang (2019)	Huang (2020)
CMCC-CM2-SR5	CMCC	1 x 1	r11p1f1	Lovato and Peano (2020)	Lovato and Peano (2020)
CMCC-ESM2	CMCC	1 x 1	r11p1f1	Lovato et al. (2021)	Lovato et al. (2021)
CNRM-CM6-1	CNRM-CERFACS	1 x 1	r11p1f2	Voldoire (2019)	Voldoire (2019)
CNRM-ESM2-1	CNRM-CERFACS	1 x 1	r211p1f2	Seferian (2018)	-
CanESM5	CCCma	1 x 1	r11p1f1	Swart et al. (2019)	Swart et al. (2019)
EC-Earth3	EC-Earth Consortium	1 x 1	r11p1f1	EC-Earth Consortium (2021)	EC-Earth Consortium (2019)
FIO-ESM-2-0	FIO-QLNM	1 x 1	r11p1f1	Song et al. (2019)	Song et al. (2019)
HadGEM3-GC31-LL	MOHC	1 x 1	r11p1f3	Ridley et al. (2019)	Good (2020)
HadGEM3-GC31-MM	MOHC	0.25 x 0.25	r11p1f3	Ridley et al. (2019)	Ridley et al. (2019)
IPSL-CM6A-LR	IPSL	1 x 1	r11p1f1	Boucher et al. (2021)	Boucher et al. (2019)
MPI-ESM1-2-HR	MPI	0.4 x 0.4	r11p1f1	Jungclaus et al. (2019)	Schupfner et al. (2019)
MPI-ESM1-2-LR	MPI	1.5 x 1.5	r11p1f1	Wieners et al. (2019)	Wieners et al. (2019)
MRI-ESM2-0	MRI	1 x 0.5	r11p1f1	Yukimoto et al. (2019)	Yukimoto et al. (2019)
NESM3	NUIST	1 x 1	r11p1f1	Cao and Wang (2019)	Cao (2019)
UKESM1-0-LL	MOHC	1 x 1	r11p1f2	Tang et al. (2019)	Good et al. (2019)

3. Methods

First, a cross section between Florida and the African continent at a latitude closest to 26°N was selected for each model. For this, mask files created from the model data were used. Masks show values of 0 where a variable has no value, all other grid cells have a value of 1. For some models, both the mask and model grid were shifted to make sure the Atlantic Ocean was located in the middle of the grid. To align the mask and model grid, the mask of models with halo points were shifted one cell to the east, as halo points were already removed in the mask files. Additionally, the mask of MPI-ESM1-2-LR and MPI-ESM1-2-HR are flipped in a north-south direction so that the mask and model grid overlap. Only model MRI-ESM2-0 revealed a mismatch between the mask and model grid for three bottom grid cells for reasons still unknown. These three grid cells were manually removed from the cross section.

A 2D cross section is selected along the latitude closest to 26°N (ilat), where longitudes closest to -80° (ilon min) and -10° (ilon max) act as the western and eastern boundary, respectively (Figure 2, left). For some models, small changes in these indices were made to make sure the east boundary crosses Florida and the west boundary crosses the African continent (Figure 2, right).

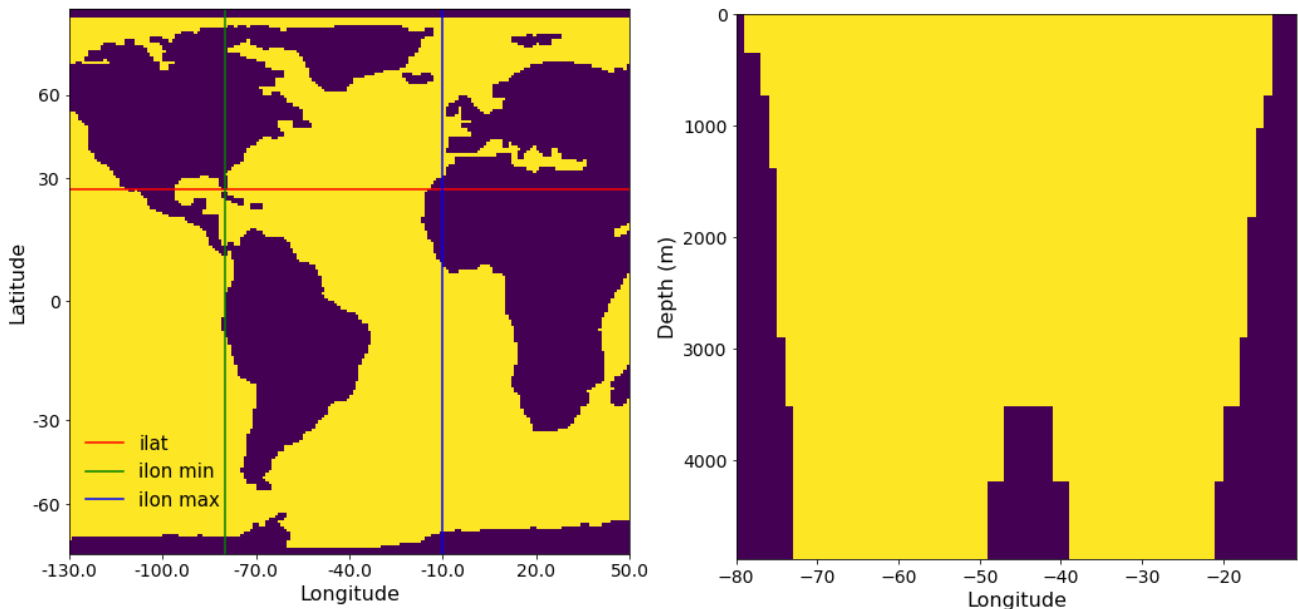


Figure 2: Mask of CAS-ESM2-0, with *ilat* (26°N), *ilon min* (-80°) and *ilon max* (-10°) indicated by the red, green and blue line respectively (left). The corresponding cross section is shown too (right).

For both the historical and SSP585 run of every model, values of the following time-varying variables along this 2D cross section were written to a file: meridional velocity (“*vo*”), zonal wind stress (“*tauuo*”), salinity (“*so*”) and potential temperature (“*thetao*”). The location of the data point within a grid cell is not the same for every variable. This location depends on the grid type of the model. The data points of the variables were averaged in such a way that their location within a grid cell overlapped with the location of the corresponding “*vo*”-point. As an example, consider the B-grid shown in Figure 3 (left). In such a grid, the “*vo*”-point and “*tauuo*”-point overlap (indicated by *v* and *u*, respectively). Also, the “*thetao*”-point and “*so*”-point have the same location (indicated by *q*). Note that the *q*-point of all four grid cells in shown in the figure. In this example, the *u,v*-point is located top right of the corresponding *q*-point. To find the value of *q* at the location of the *u,v*-point, we average the *q*-value of the grid cell with those of the grid cells located at the top, top-right and on the right of our grid cell.

As a second example, consider the C-grid shown in Figure 3 (right). In contrast to the B-grid, the v- and u-point do not overlap in this a grid. Note that the u-point of all four grid cells is shown in this figure, while the q-point of our grid cell and the one above (i+1,j) is shown. Thus, both the q- and u-point need to be averaged to obtain these values at the same location as the v-point. In this case, we average the q-value of the grid cell with the grid cell above and we average the u-value of the grid cell with those of the grid cells located at the top, top-left and left of our grid cell.

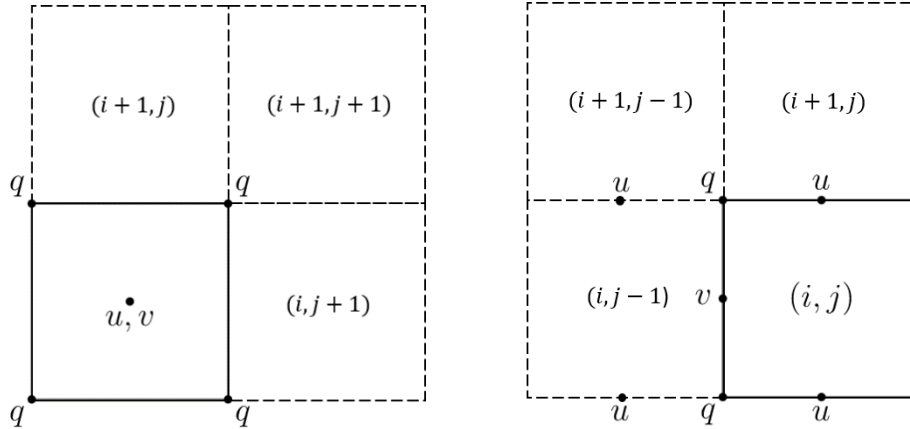


Figure 3: Example of a Btr-grid cell (left) and a Ctr-grid cell (right) indicated by the solid line. The “tauuo”- and “vo”-point are indicated by u,v and the “thetao”- and “so”-point by q.

Furthermore, the following non-varying variables are added to the file: time, longitude, latitude, depth and both width (dx) and height (dz) of each grid cell.

Then, the transport through each grid cell is calculated by multiplying the meridional velocity with the size (dx*dz) of the cell. The net transport through the section is approximately -1 Sv for every model (Appendix A). This non-zero net transport is caused by input of water from the north through the Bering Strait of the same amount. Due to this input into the Arctic Ocean, the southward transport exceeds the northward transport at 26°N, resulting in a negative net transport. To maintain a net meridional transport of zero through the cross section, transport of each grid cell is corrected for this throughflow based on the grid size. Thus, the corrected transport through each grid cell (tp_c) is:

$$tp_c = tp_{nc} - (tp_{net} * A_{gc} / A_{tot})$$

Where tp_{nc} is the transport through the grid cell before correction, tp_{net} the net transport through the total cross section, A_{gc} the area of the grid cell and A_{tot} the area of the total cross section. This is done for every timestep, to obtain a net meridional transport of zero through the cross section for each model (Appendix A). The corrected transport is summed zonally and cumulated from bottom to top to obtain the overturning stream function:

$$\Psi(z) = \int_z^0 \int_{x_w}^{x_e} v \, dx \, dz$$

Where v is the meridional velocity (thus $v \, dx \, dz$ is equal to the meridional transport), x_w and x_e are the western and eastern boundary, respectively, and z is the ocean depth. Since the stream function is a cumulative sum from bottom to top, it is a function of depth (z). For some models the overturning stream function is part of the output data, in which case the calculated stream function

could be evaluated. Additionally, the total transport is decomposed into the following transport components: Florida Straits, Ekman, thermocline recirculation, intermediate water, upper North Atlantic Deep Water, lower North Atlantic Deep Water and Antarctic Bottom Water.

The boundaries between these components are based on transport and potential temperature characteristics (Figure 4). The horizontal lower boundary of Florida Straits (FS) transport is the depth of maximum overturning (i.e. ψ_{max}). The vertical boundary between FS and mid ocean transport is defined as the longitude where the depth-averaged transport above the depth of maximum overturning changes from positive (northward) to negative (southward), on the condition that this boundary lies east of the depth-averaged maximum. The boundary between thermocline recirculation (tr) and intermediate water (iw) is set at a horizontally averaged potential temperature of 8 °C. The depth of maximum overturning is used as the boundary between intermediate water and upper North Atlantic Deep Water (NADW) and a horizontally average potential temperature of 3 °C is used to divide upper and lower NADW. Finally, the boundary between lower NADW and Antarctic Bottom Water (AABW) is defined as the depth where horizontally averaged transport changes from negative to positive, meaning AABW is defined as northward flowing bottom water. The definition of the two boundaries based on potential temperature characteristics originates from previous studies (e.g. Frajka-Williams et al., 2011). All boundaries are allowed to vary in time, so they are computed for every timestep.

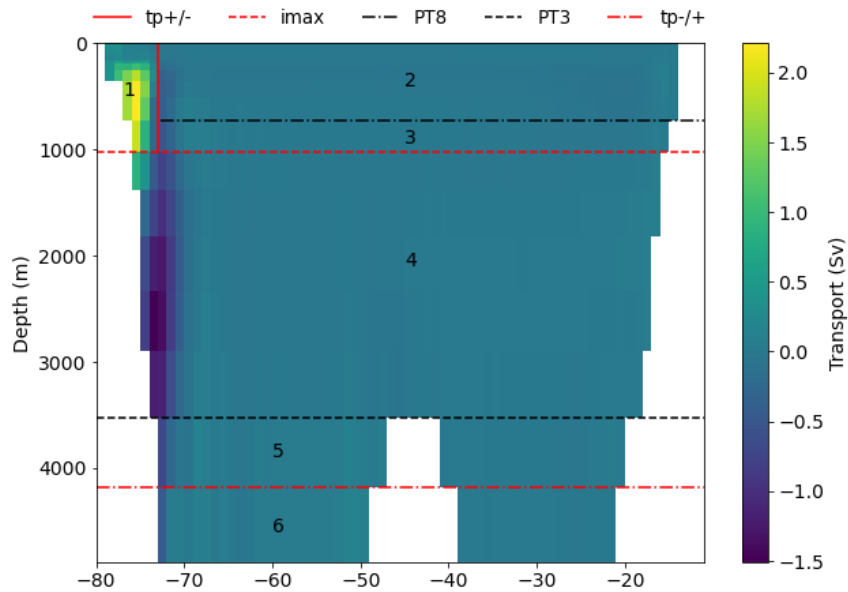


Figure 4: Historical mean transport through the cross section for CAS-ESM2-0. Boundaries between transport components are illustrated by black and red lines. 1 = FS, 2 = tr, 3 = iw, 4 = upper NADW, 5 = lower NADW, 6 = AABW.

Ekman surface transport is calculated from the zonal wind stress, using the theoretical relationship

$$tp_{ek} = \frac{-\tau_x}{f\rho} dx$$

Where τ_x is the zonal wind stress, f the Coriolis parameter at 26°N and ρ is the water density. Hence, thermocline recirculation is defined as the transport above the PT = 8 °C boundary minus Ekman transport. It is important to note that, since the Bahamas are absent in most models (Figure

4), northward transport east of the Bahamas by the Antilles Current is included in the Florida Straits component.

Additionally, the NADW component is divided into two parts to examine the circulation of deep-water: the deep western boundary current (DWBC) and interior flow. The boundary between these parts is defined as the longitude at which the depth-averaged NADW transport shifts from negative to positive, under the condition that it is placed east of the location where the depth-averaged southward transport is maximum.

Not only the strength but also the variability of the transport components is analysed. The total variability is compared to the mean transport and the variability is decomposed into three components: low-frequency, seasonal and high-frequency variability. This is done using the Python function `seasonal_decompose` of the `statsmodels` module. This function first estimates the trend (low-frequency) by applying a convolution filter, which is then removed from the timeseries. The detrended timeseries is averaged for every period to obtain the seasonal component, where the total seasonal period is 12 months. For example, the value of the seasonal component for January is the average of all January values in the timeseries. The residual (high-frequency), is the remainder which is not explained by the trend or seasonal component. These components indicate the interannual (low-frequency), seasonal and weekly to monthly (high-frequency) variability. An example of the decomposed timeseries of the total MOC is shown in Appendix B. The Pearson's correlation coefficient is obtained to examine relationships between the decomposed variability of transport components.

In Chapter 5, we discuss the effect of changes in wind stress curl on the future decline of the components and relate future AMOC decline to historical sea ice extent and seasonality. In order to quantify changes in wind stress curl, we computed the mean curl along the 26°N section for the historical and SSP585 period. We first extracted the meridional wind stress (“ τ_y ”) from the model output. Then, the wind stress curl around every “vo”-point is computed for every model using:

$$\text{curl } \tau = d\tau_y/dx - d\tau_x/dy$$

Where τ_y is the meridional wind stress and τ_x is the zonal wind stress. Again, averaging is needed to compute the wind stress curl at the correct location. The mean wind stress curl along the section is analysed for every timestep.

To obtain historical sea ice extent and seasonality, we used the percentage of each grid cell covered by sea ice (“ $siconc$ ”). Only Northern Hemisphere sea ice cover above 40°N is analysed. To correct for variations in grid cell size, we multiplied the percentage of sea ice cover with the area of every grid cell (“ $areacello$ ”). Only NESM3 did not include this variable in their output data. Since the sea ice data of this model is plotted on a distinct sea ice grid, we are unable to obtain values for the grid cell area. Therefore, NESM3 is excluded from this analysis. The standard deviation of the mean is used to indicate seasonality.

In Appendix C, three examples are shown of method considerations used in this study and their impact on the obtained transport. The first example displays the effect of removing the halo points on the net transport through the section. The other two examples are related to the conditions for the selection of boundaries between transport components.

4. Results

In the first section of this chapter, we compare model data with observational estimates for the historical period. In the second section, future projections under SSP585 are shown and we compare the historical mean state with future changes. All standard errors of the means are based on the standard deviation normalized with the square-root of the number of observations for the 95% confidence interval. Transport values are given in Sverdrup (Sv), where 1 Sv is equal to 1 million m^3/s .

4.1 Comparing historical model data with observational estimates

In this section, we compare historical data of CMIP6 models with observed RAPID data. To assess the representation of the mean overturning strength and structure, we compare the modelled and observed overturning stream function, since it clearly portrays potential model biases and inter-model differences of the overturning circulation. Hereafter, we assess how well models are able to reproduce the different transport components by analysing the timeseries of each component. From this, we could gain insight into the potential drivers of differences between RAPID and CMIP6 data. Additionally, we analyse the structure of the AMOC at 26°N in more detail by discussing the circulation of deep-water. Not only the strength, but also the variability of each transport component is analysed. We plot the total variability against the historical mean of each component to determine whether models that are able to reproduce the strength of a particular component, also reproduce the variability correctly. Furthermore, the variability is decomposed into low-frequency, seasonal and high-frequency variability to analyse similarities and differences with observations on different timescales. Finally, we show correlations between the transport components on each timescale. This enables us to verify if components with a similar variability are correlated over time.

4.1.1 Overturning stream function

The calculated overturning stream function is similar to the one included in the output data of several models (Appendix D). The overturning transport for the overlapping time period (April 2004 - December 2014) shows a higher mean for observational data than for modelled data with values of 17.0 ± 0.9 Sv and 14.6 ± 0.2 Sv, respectively (Figure 5). One clear outlier with relatively low overturning values is NESM3. There are large inter-model differences in mean AMOC strength with a maximum difference of 9.4 Sv between NESM3 and CAS-ESM2-0 (Appendix E). Of the 19 models, 4 models are able to reproduce the mean AMOC strength within one standard error of the RAPID data: CESM2-WACCM, EC-Earth3, FIO-ESM-2-0 and MPI-ESM1-2-LR (Appendix G). Several models show a depth of maximum overturning close to the observed 1031 m, but most models capture a shallower depth with an ensemble mean of 949 ± 58 m. The NADW cell is relatively shallow in models, which results in AABW being present over a larger depth interval. The ensemble mean depth of the boundary between NADW and AABW is 3993 ± 148 m, while for RAPID data this depth is 5065 m. Note that the standard error of the overturning transport is based on the time series of each model, while the standard error of depth boundaries shows the inter-model variability (i.e. deviation of each model mean from the ensemble mean).

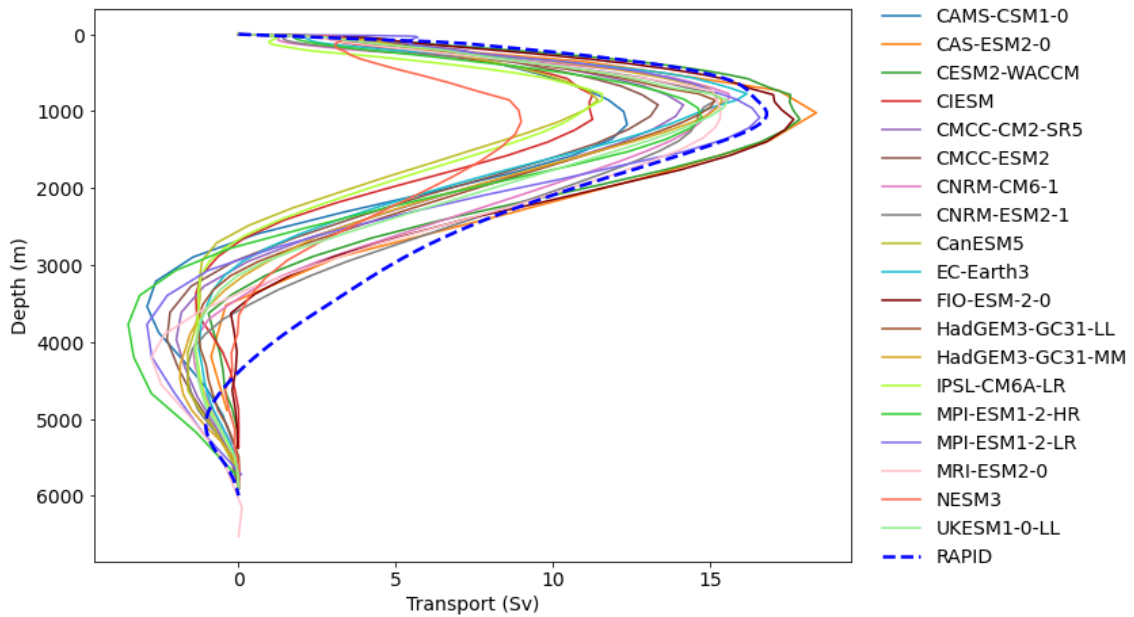


Figure 5: Historical mean overturning stream function of the models analysed. The overturning stream function of RAPID data is shown by the dashed blue line.

4.1.2 Timeseries of components

Above, the strength of the total MOC is discussed. Here we examine the observed and modelled strength of each transport component during the historical period (Figure 6). For the transport above the depth of maximum overturning, RAPID estimates yield a mean northward transport through the Florida Straits of 31.3 ± 0.4 Sv, northward Ekman transport of 3.6 ± 0.4 Sv, southward thermocline recirculation of -18.6 ± 0.5 Sv and minor northward intermediate water transport of 0.4 ± 0.1 Sv. Thus, the net northward transport of the upper limb is 16.8 ± 0.6 Sv. Below the depth of maximum overturning, RAPID shows a mean southward transport of upper and lower NADW of -11.9 ± 0.3 Sv and -5.9 ± 0.4 Sv, respectively. Hence, the total southward transport of the lower limb is -17.8 ± 0.6 Sv. Additionally, 1.0 ± 0.1 Sv AABW is transported northward at the bottom.

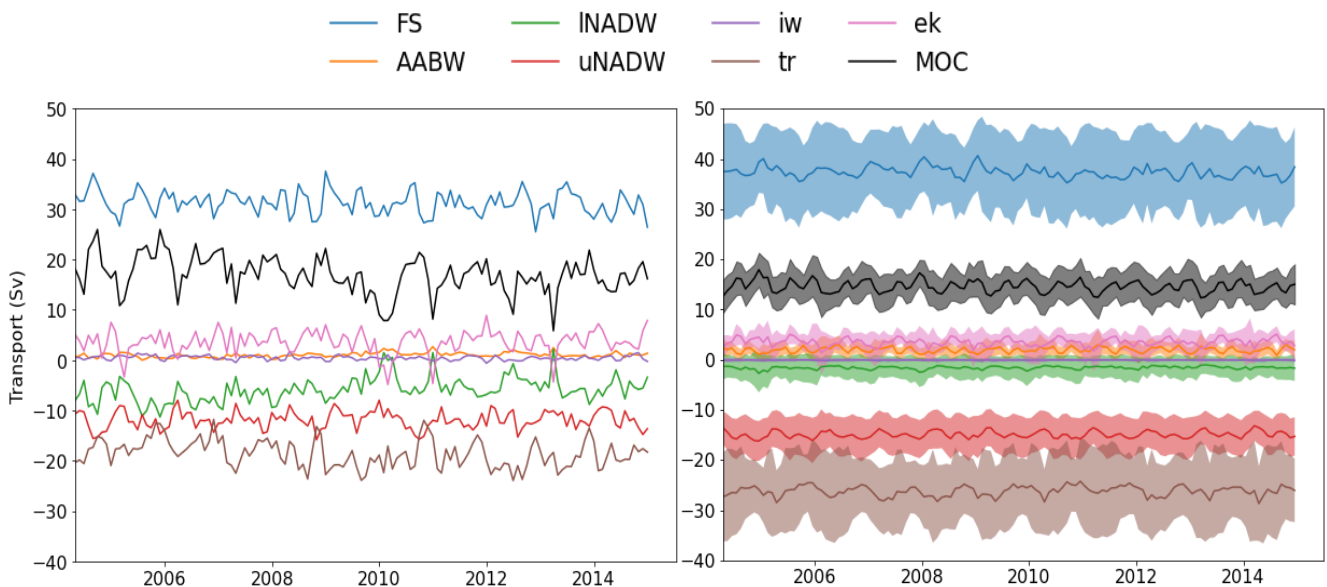


Figure 6: Historical timeseries for RAPID data (left) and ensemble mean CMIP6 data (right). The shaded areas indicate one standard deviation of the ensemble spread.

The CMIP6 ensemble mean transport of most components differs significantly from RAPID estimates for the historical period (Figure 6). For the upper ocean transport, the ensemble mean shows northward transport through the Florida Straits of 37.4 ± 0.2 Sv, northward Ekman transport of 3.5 ± 0.1 and southward thermocline recirculation of -26.2 ± 0.2 Sv. Models were unable to correctly reproduce transport of intermediate water. Thus, the resulting net transport of the upper limb is 14.6 ± 0.2 Sv. Even though Florida Straits transport is significantly higher than observed, more water is recirculated southward resulting in less northward upper-ocean transport compared to RAPID. Below the depth of maximum overturning, models yield a mean southward transport of upper and lower NADW of -14.9 ± 0.1 Sv and -1.6 ± 0.1 Sv, respectively. The total lower limb transport of -16.5 ± 0.1 Sv is lower than observed as well, due to significantly less lower NADW transport in models. At the bottom, 1.9 ± 0.1 Sv AABW is transported northward.

Over the historical period, RAPID estimates show a significant decline in Florida Straits, lower NADW and total MOC transport. An increase can be observed for thermocline recirculation and AABW. The CMIP6 ensemble mean only reproduces the decline in Florida Straits transport and lower NADW. Since the analysed record spans just 11 years, we are unable to attribute these changes to either a long-term trend or decadal variability. Like for the total MOC, large inter-model differences are present in the historical mean of the transport components (Appendix E). The spread ranges from 3.0 Sv for AABW to 28.5 Sv for thermocline recirculation. For several components (tr, INADW and AABW), the inter-model spread is higher than their ensemble mean.

Since models are unable to reproduce intermediate water, this component is not used in further analysis. Additionally, the modelled INADW is significantly lower than observed by the RAPID array. Therefore, uNADW and INADW are combined and analysed as one components named NADW.

4.1.3 Deep-water circulation

To examine the circulation of deep-water, the NADW component is split into a DWBC and interior transport (Figure 7). Over the historical period, the mean transport of the DWBC is -17.5 ± 0.5 Sv with an inter-model spread of 13.7 Sv. The interior part of NADW has a mean of 1.0 ± 0.5 Sv with a large inter-model spread of 9.3 Sv. Recent estimates from RAPID data yield much higher values for both components, with DWBC transport of -28 Sv and 10 Sv recirculation in the interior (Bryden, 2021). Interestingly, both components show a large seasonal signal, where a weaker DWBC is compensated by southward interior transport. Maxima of both components occur in September and minima in January.

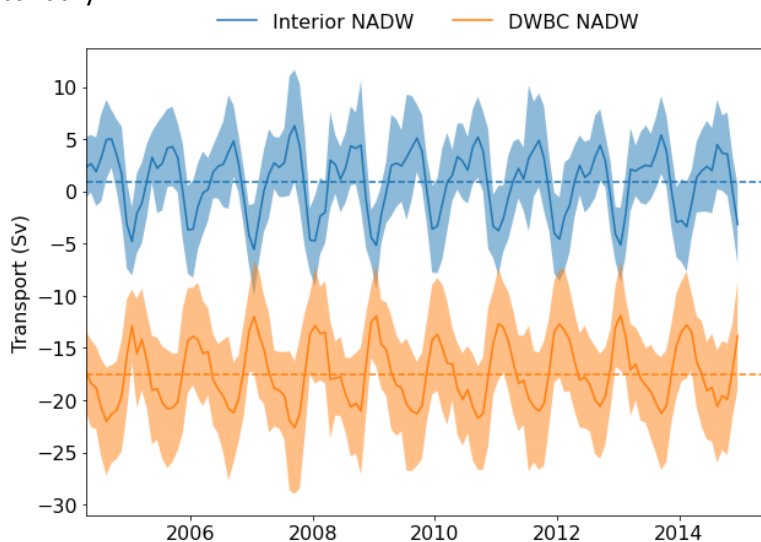


Figure 7: Historical timeseries of the DWBC and interior NADW transport. Shaded areas indicate one standard deviation of the inter-model spread.

To further analyse the structure of NADW transport, we examined the historical mean transport below the depth of maximum overturning through the cross section for all models. Additionally, NADW transport is summed vertically for every longitude. Below, an example is shown for the model UKESM1-0-LL (Figure 8). A distinct southward flowing DWBC is observed in all models. Most models show a width of around 300 km, which is two times broader than estimated from observations (e.g. Bryden, 2021). The location of the DWBC maximum ranges from -76.5° to -72° longitude. Partial recirculation occurs predominantly east of this current around -70° longitude. Additionally, most models show southward transport via interior pathways: along the east side of the Mid-Atlantic Ridge and west of the eastern boundary. However, southward transport at these locations is substantially smaller than in the DWBC. Minor northward transport occurs east of the Mid-Atlantic Ridge as well.

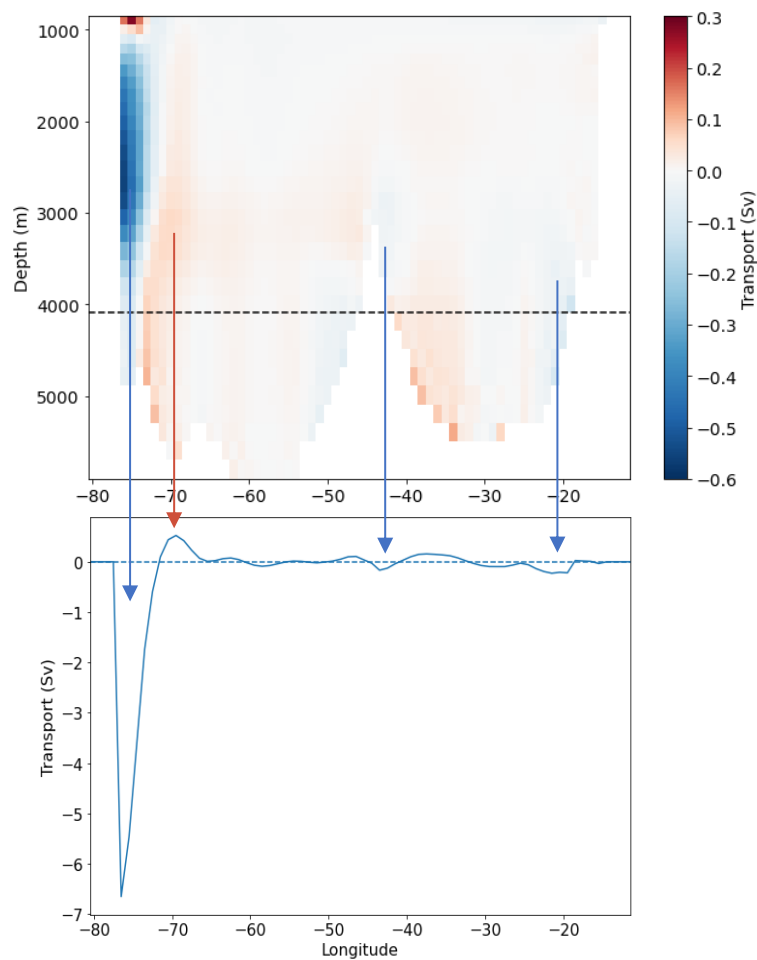


Figure 8: Historical mean transport below the depth of maximum overturning through the cross section for UKESM1-0-LL (upper). Vertically summed NADW transport for the same model (lower).

4.1.4 Total variability of components

When comparing the historical mean and standard deviation of each model with observed data, we can examine whether models are able to reproduce the natural variability of the different components and if this is related to their ability to reproduce the historical mean (Figure 9).

For Florida Straits transport, the ensemble mean variability (2.9 Sv) is somewhat higher than observed (2.3 Sv). MPI-ESM1-2-HR shows a variability that is 4 times higher than the ensemble mean. When excluding this outlier, the ensemble mean reduces to 2.4 Sv, a variability more similar to observation. The ensemble mean variability of Ekman transport (2.2 Sv) is similar to the observed value (2.3). Again, the variability of MPI-ESM1-2-HR is significantly higher than the other models. When excluding this model, the ensemble mean variability becomes 2.1 Sv. For thermocline recirculation, the ensemble mean variability (2.7 Sv) is also close to the observed mean (2.8 Sv). Like for Florida Straits transport, the variability of MPI-ESM1-2-HR is higher than the ensemble mean by a factor 4. The ensemble mean drops significantly to a value of 2.1 Sv when excluding this model. The ensemble mean variability of NADW (1.8 Sv) is almost half of the observed mean (3.3 Sv). Both upper and lower NADW yield a variability lower than observed (not shown). AABW is the only component that shows an ensemble mean variability (1.5 Sv) that is much higher than observed (0.5 Sv). Additionally, the variability decreases with lower historical mean values. Thus, models with a lower and more accurate historical mean yield a variability closer to observations. However, the difference is still a factor 2. Note that the mean variability is not related to the mean strength for the other components. For the total MOC, the ensemble mean variability (2.6 Sv) is significantly lower than RAPID estimates (3.7 Sv). Excluding MPI-ESM1-2-HR, which proved to be an outlier in 3 of the 5 components, results in a minor decrease of the ensemble mean to a value of 2.5 Sv. However, the total variability is a product of variability on different timescales. Thus, to examine the variability in different frequency domains, decomposition of the total variability is required.

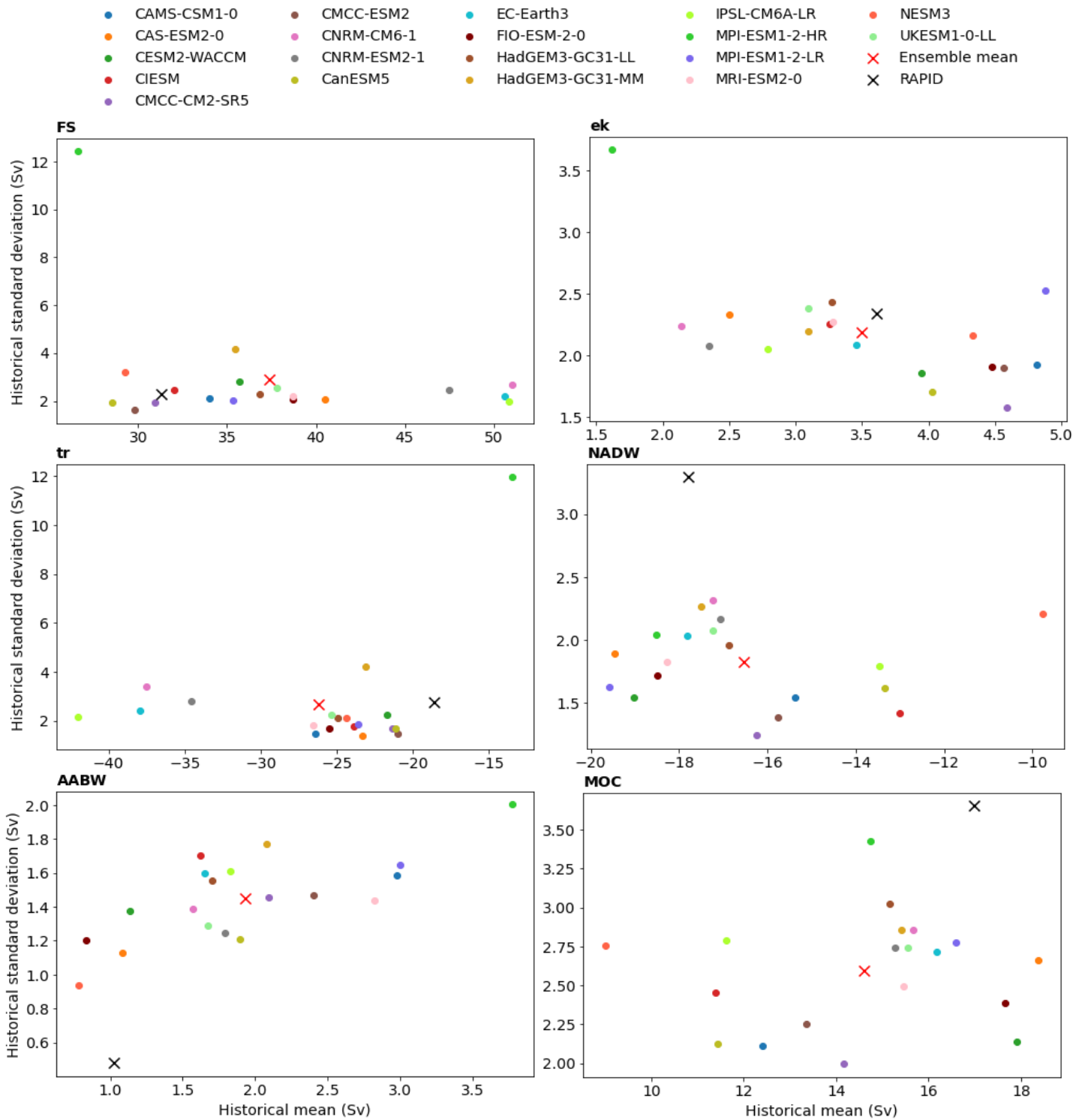


Figure 9: Historical mean standard deviation against historical mean strength of each model. The ensemble mean and RAPID mean are indicated by the red and black cross, respectively.

4.1.5 Decomposition of variability

As mentioned in the prior section, decomposition of the total variability is required to obtain insight into the variability on different timescales. The results of the decomposition are shown in this section. The total variability is decomposed into three components: low-frequency (interannual), seasonal and high-frequency (weekly to monthly) variability (Figure 10).

Generally, the standard deviation of each variability component is in line with the total variability for each transport component. For example, NADW showed a lower total variability than observed (Figure 9) and the ensemble means of the different variability components for NADW are all lower than the RAPID mean (Figure 10). However, the total variability of Florida Straits transport has an ensemble mean comparable to observations, but the low-frequency and seasonal variability are both significantly higher than observed. The high-frequency variability for this transport component is lower than the RAPID mean. The total, low-frequency and seasonal variability of thermocline recirculation are reproduced very well by the models, but the ensemble mean of high-frequency variability is somewhat lower than observed. It is interesting to note that even though total, high and low-frequency variability of the MOC are significantly lower than observed, the ensemble mean seasonal variability is comparable to observations. Like for the total variability, MPI-ESM1-2-HR shows extremely high values for Florida Straits transport and thermocline recirculation on all timescales. When excluding this model, Florida Straits variability remains overestimated on low-frequency and seasonal timescales and variability of thermocline recirculation becomes lower than the observed mean for all timescales (Appendix G).

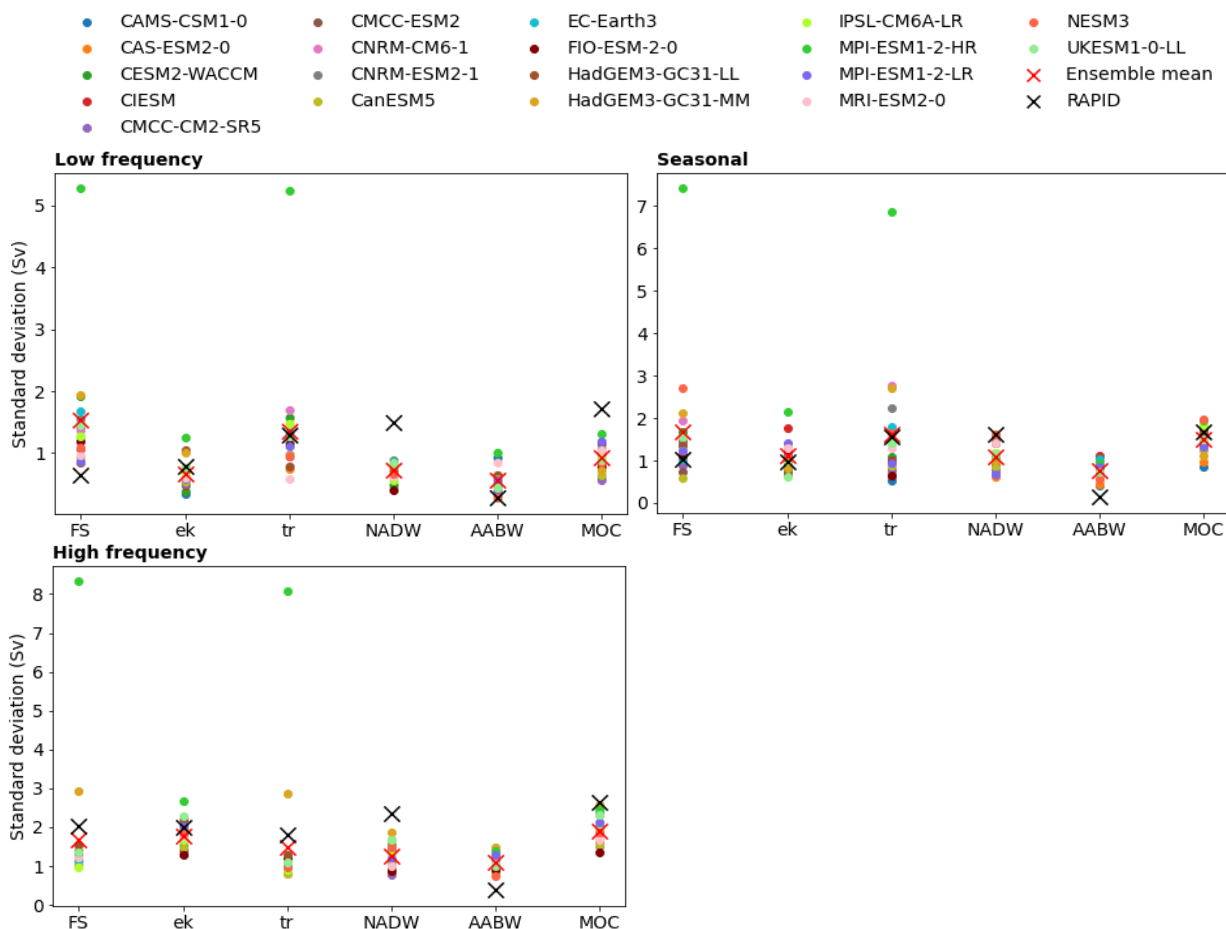


Figure 10: Decomposed variability of each transport component into low-frequency, seasonal and high-frequency variability. The ensemble mean and RAPID mean are indicated by the red and black cross, respectively.

The low-frequency and seasonal variability are dominated by Florida Straits transport and thermocline recirculation in models, but NADW and thermocline recirculation are the largest contributors on these timescales in the observed data. Ekman transport is the component with the largest high-frequency variability in models, while this is NADW for observational data. The multi-model ensemble mean is generally higher for high-frequency variability than seasonal variability, and the ensemble mean of low-frequency variability is lower than both. Only for Florida Straits transport and thermocline circulation the ensemble mean seasonal variability exceeds high-frequency variability. For RAPID estimates, the only exceptions to this rule (high-frequency > seasonal > low-frequency) are AABW and total MOC, where low-frequency variability exceeds seasonal variability.

Relationships between the decomposed variability of different transport components are examined using a Pearson's correlation. At all three timescales, correlations between transport components of observed and modelled data are compared. Only significant strong correlations with a coefficient higher than (-)0.7 are discussed (Table 2 and 3). A table with all correlation coefficients is shown in Appendix F. Red values indicate disagreement between the observed and modelled correlation, that is where observations show a significant correlation coefficient of (-)0.7 or higher and the models yield a coefficient lower than this threshold or vice versa. As expected, RAPID shows an almost perfect correlation between NADW and MOC (-0.99) on all three time scales. Models also show a strong correlation of -0.81 (low-frequency), -0.86 (seasonal) and -0.82 (high-frequency). However, RAPID data shows that the MOC is also correlated with thermocline recirculation (0.83) and AABW (-0.89) for low-frequency variability, with Ekman (0.77) on a seasonal time scale and with AABW (-0.81) and Ekman (0.72) for high-frequency variability. Most of these correlations are reproduced by CMIP6 models, with some correlation coefficients just below (-)0.7. Only the correlation between MOC and thermocline recirculation varies from RAPID observations, with a coefficient of -0.09. Since NADW and MOC are almost perfectly correlated in RAPID data, similar results are found when comparing NADW with the above mentioned components. For models, correlations with NADW are much weaker. Only Ekman transport shows a strong correlation (-0.76) in the high-frequency domain. Interestingly, models show a correlation between thermocline recirculation and FS for low-frequency (-0.84), seasonal (-0.70) and high-frequency (-0.76) variability, while RAPID data does not show this correlation for low-frequency variability (0.06). Note that the correlation coefficient between FS and thermocline recirculation is only negative due to a difference in transport direction. Thus, when northward Florida Straits transport increases, more southward thermocline recirculation occurs.

Table 2: Pearson's correlation coefficients for RAPID data.

	<i>Low-frequency</i>	<i>Seasonal</i>	<i>High-frequency</i>
<i>MOC</i>	NADW (-0.99) AABW (-0.89) tr (0.83)	NADW (-0.99) ek (0.77) AABW (-0.66)	NADW (-0.99) AABW (-0.81) ek (0.72)
<i>NADW</i>	tr (-0.85) AABW (0.85)	ek (-0.73)	AABW (0.77) ek (-0.71)
<i>tr</i>	NADW (-0.85) FS (0.06)	FS (-0.74)	FS (-0.56)

Table 3: Pearson's correlation coefficients for CMIP6 models.

	<i>Low-frequency</i>	<i>Seasonal</i>	<i>High-frequency</i>
<i>MOC</i>	NADW (-0.81)	NADW (-0.86)	ek (0.90)
	AABW (-0.63)	AABW (-0.70)	NADW (-0.82)
	tr (-0.09)	ek (0.69)	AABW (-0.77)
<i>NADW</i>	AABW (0.12)	ek (-0.55)	ek (-0.76)
	tr (0.05)		AABW (0.29)
<i>tr</i>	FS (-0.84)	FS (-0.70)	FS (-0.76)
	NADW (0.05)		

4.2 SSP585 model data

In this section, we examine the future projections of the AMOC under SSP585. First, we discuss the overturning stream function for the last decade of the 21st century and compare it to the modelled overturning circulation of the historical period. The timeseries of the transport components are analysed as well. This allows us to assess which of the components dominate future AMOC changes. Additionally, we discuss the deep-water circulation and compare it to the historical period to examine changes in the horizontal structure of the abyssal circulation. Finally, we plot the change under SSP585 against the historical mean of each components in order to find potential “emergent constraint” relationships.

4.2.1 Overturning stream function

The mean overturning stream function for the time period 2090-2100 is shown in Figure 11. Clearly, the maximum overturning is lower than for the historical period, with a mean of 8.0 ± 0.2 Sv. Also, large inter-model differences with a spread of 9.8 Sv can be observed. Both the depth of maximum overturning (807 ± 7 m) and the boundary between NADW and AABW (3261 ± 26 m) are shallower than for the historical period.

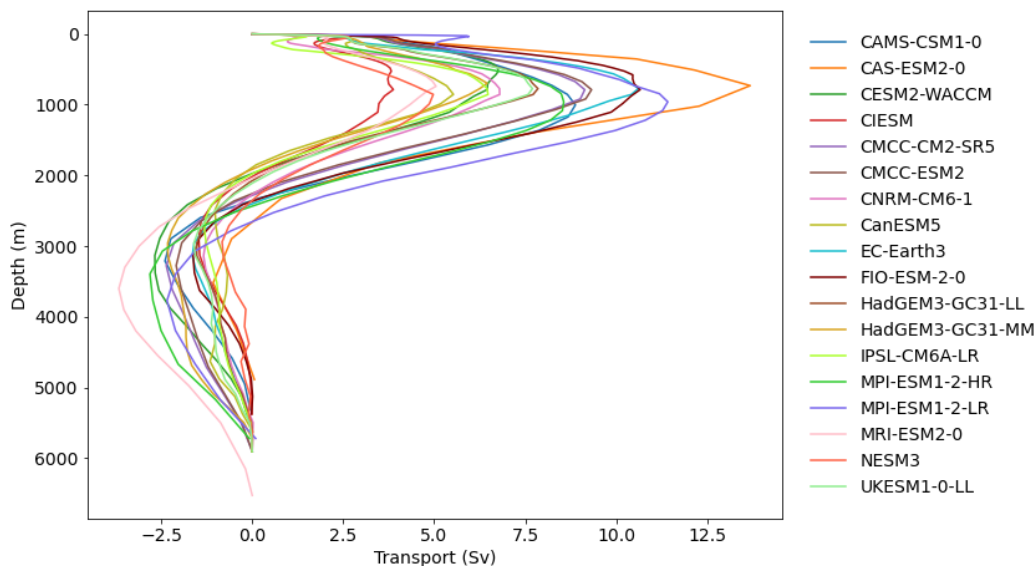


Figure 11: Mean overturning stream function for the last decade of SSP585 (2090-2100).

4.2.2 Timeseries of components

In scenario SSP585 the ensemble mean of almost all components decreases slightly until 2025, after which a more rapid decline is visible (Figure 12). We define the future decline as the difference in mean transport between the last decade of SSP585 (2090-2100) and the historical period, divided by the historical mean. For the upper limb, the ensemble mean shows a decline in Florida Straits transport of 11.0 Sv (-30%) and in thermocline recirculation of 4.4 Sv (-17%). Ekman transport shows a minor increase of 0.04 Sv (1%). Like in the historical run, models are unable to reproduce intermediate water correctly. Since Florida Straits transport and thermocline recirculation have opposing transport directions, the net decrease of northward upper-ocean transport is 6.6 Sv. For the lower limb, upper and lower NADW show a decline of 5 Sv (-34%) and 1.4 Sv (-85%), respectively. This results in a net decline in southward transport of 6.4 Sv. Since the net transport through the section is 0, the difference between upper and lower limb decline is compensated by increased AABW transport of 0.2 Sv (9%). The decline of ensemble mean MOC transport is 6.6 Sv (-45%), with significant inter-model differences in absolute and relative decline (Appendix G). However, all models show a decrease compared to the historical time period, ranging from -26% (CAS-ESM2-0) to -67%

(MRI-ESM2-0). The change of the transport components shows large inter-model differences as well, with a spread ranging from 1.4 Sv for Ekman to 13.8 Sv for Florida Straits (Appendix E). Like for the total MOC, all models show a decline in Florida Straits transport, thermocline recirculation and NADW transport. However, for Ekman and AABW transport there is disagreement between models, with both increases and decreases under SSP585.

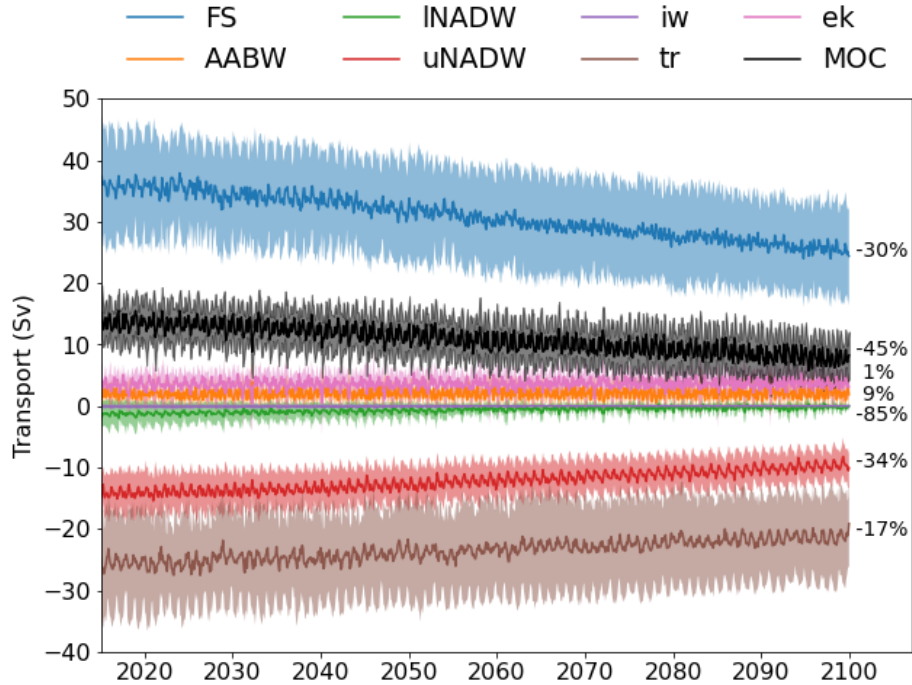


Figure 12: Ensemble mean timeseries of each component under SSP585. Shaded areas illustrate one standard deviation of the inter-model spread. Percentages show the decline relative to the historical period.

4.2.3 Deep-water circulation

If we again divide NADW into transport by a DWBC and interior flow, a decline in both components is observed (Figure 13). For the last decade of SSP585, the ensemble mean DWBC transport is -9.8 ± 0.1 Sv with an inter-model spread of 14.4 Sv. The ensemble mean interior NADW transport for this period is -0.3 ± 0.1 Sv, with an inter-model spread of 10.7 Sv. Compared to the historical mean, the DWBC and interior transport show a decline of 7.7 Sv (-43%) and 1.3 Sv (-132%), respectively. Note that the average interior transport changes from northward to southward under SSP585.

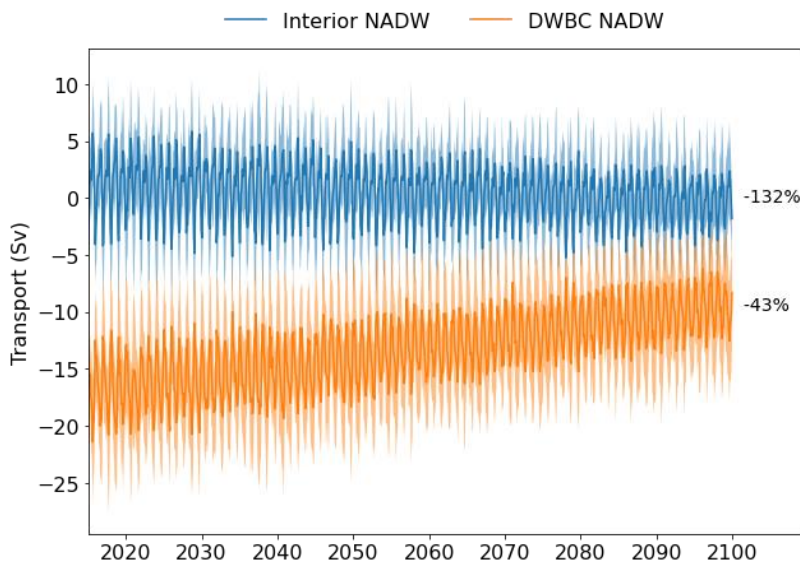


Figure 13: Ensemble mean timeseries of DWBC and interior NADW transport. Shaded areas illustrate one standard deviation of the inter-model spread. Percentages show the decline relative to the historical period.

To examine possible changes in the structure of deep-water circulation, the difference in transport through the cross section between the historical period and the last decade of SSP585 is shown for model UKESM1-0-LL. Also, the vertically summed transport for both periods is shown to display changes in the structure of NADW transport (Figure 14). All models show a decline in transport by the DWBC and several models (CAM5-CSM1-0, CAS-ESM2-0, CNRM-CM6-1, CanESM5, IPSL-CM6A-LR, MPI-ESM1-2-LR, MRI-ESM2-0, NESM3, UKESM1-0-LL) display an additional narrowing of this current. For these models, the result is a slight westward shift of the boundary between the DWBC and interior NADW transport. Most models show a decrease in the maximum northward flow just east of the DWBC, while FIO-ESM2-0, NESM3 and UKESM1-0-LL show no difference compared to the historical period. Only CAS-ESM2-0 displays an increase in this northward transport. Generally, southward transport just east of the Mid-Atlantic Ridge decreases and for some models it even shifts from southward to northward. Only CAM5-CSM1-0, CanESM5 and MPI-ESM1-2-HR show increased southward transport at this location. However, it is important to note that for several models the boundary between NADW and AABW under SSP585 is located above the Mid-Atlantic Ridge, so that the transport east of the Ridge is not included in interior NADW transport. Additionally, southward transport west of the Mid-Atlantic Ridge increases for several models (CESM2-WACCM, CIESM, CMCC-CM2-SR5, HadGEM3-GC31-LL, MRI-ESM2-0, NESM3, UKESM1-0-LL), but changes are relatively small. Therefore, the decline in interior northward transport is generally caused by a decrease in northward transport around -70° longitude, which is larger than the decline in southward transport on the east-side of the Mid-Atlantic Ridge.

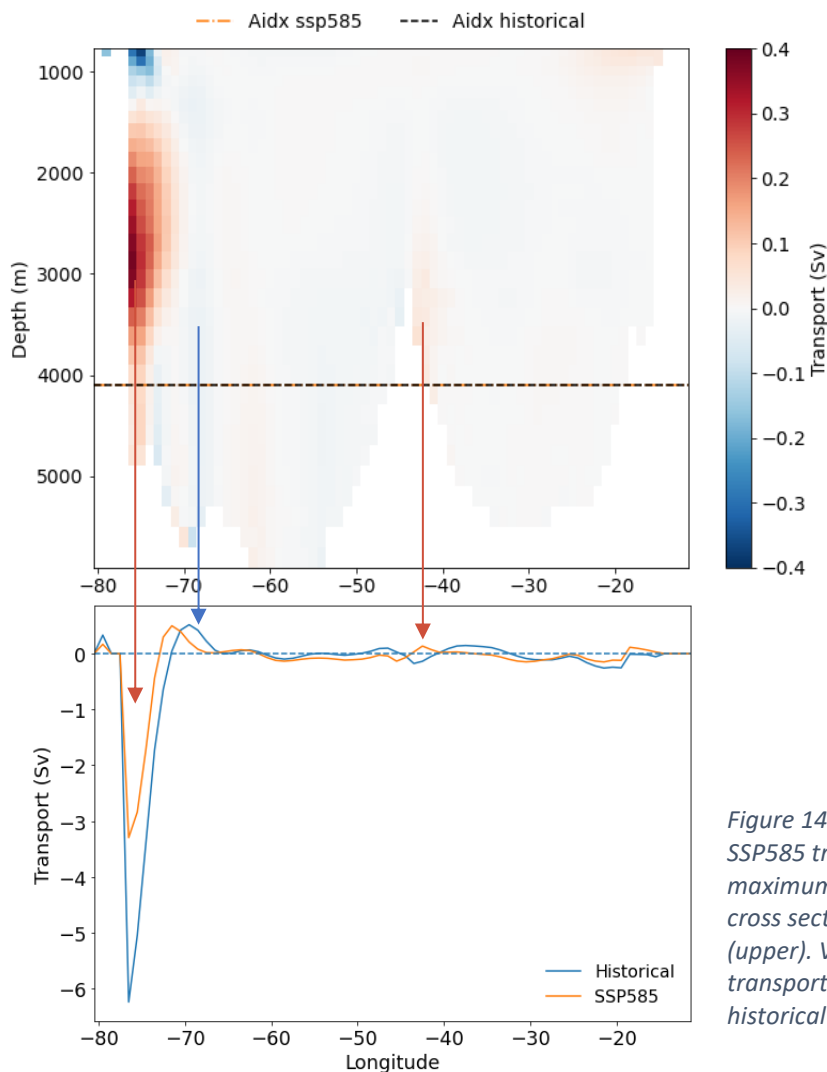


Figure 14: Difference in historical and SSP585 transport below the depth of maximum overturning through the cross section for UKESM1-0-LL (upper). Vertically summed NADW transport of the same model for the historical and SSP585 period (lower).

4.2.4 Historical mean vs SSP585 future changes

In this section, the projected change under SSP585 is compared to the historical mean of the different components (Figure 15). Again, this change is defined as the mean transport of the last decade of SSP585 (2090 – 2100) minus the mean of the historical period (2004 – 2014). This allows us to examine potential relationships between the mean state and future changes of the components. These so called emergent constraint relationships could be used to improve estimations of future change based on observational data (Hall et al., 2019).

Generally, models with a high historical mean show a larger decline in their SSP585 projection. Only for Ekman, AABW and total MOC this relationship is significant within the 90% confidence interval ($p < 0.01$). For NADW this relationship is somewhat significant with a p-value of 0.106. However, the relationship is relatively weak for all components, including the total MOC. The significance of this relation is highly dependent on which models are used. For example, when excluding the outlier CAS-ESM2-0, we find p-values below 0.05 for Ekman, AABW, NADW and MOC. However, we see no basis for the exclusion of certain models. Note that the total variability is relatively high compared to inter-model variations for most components.

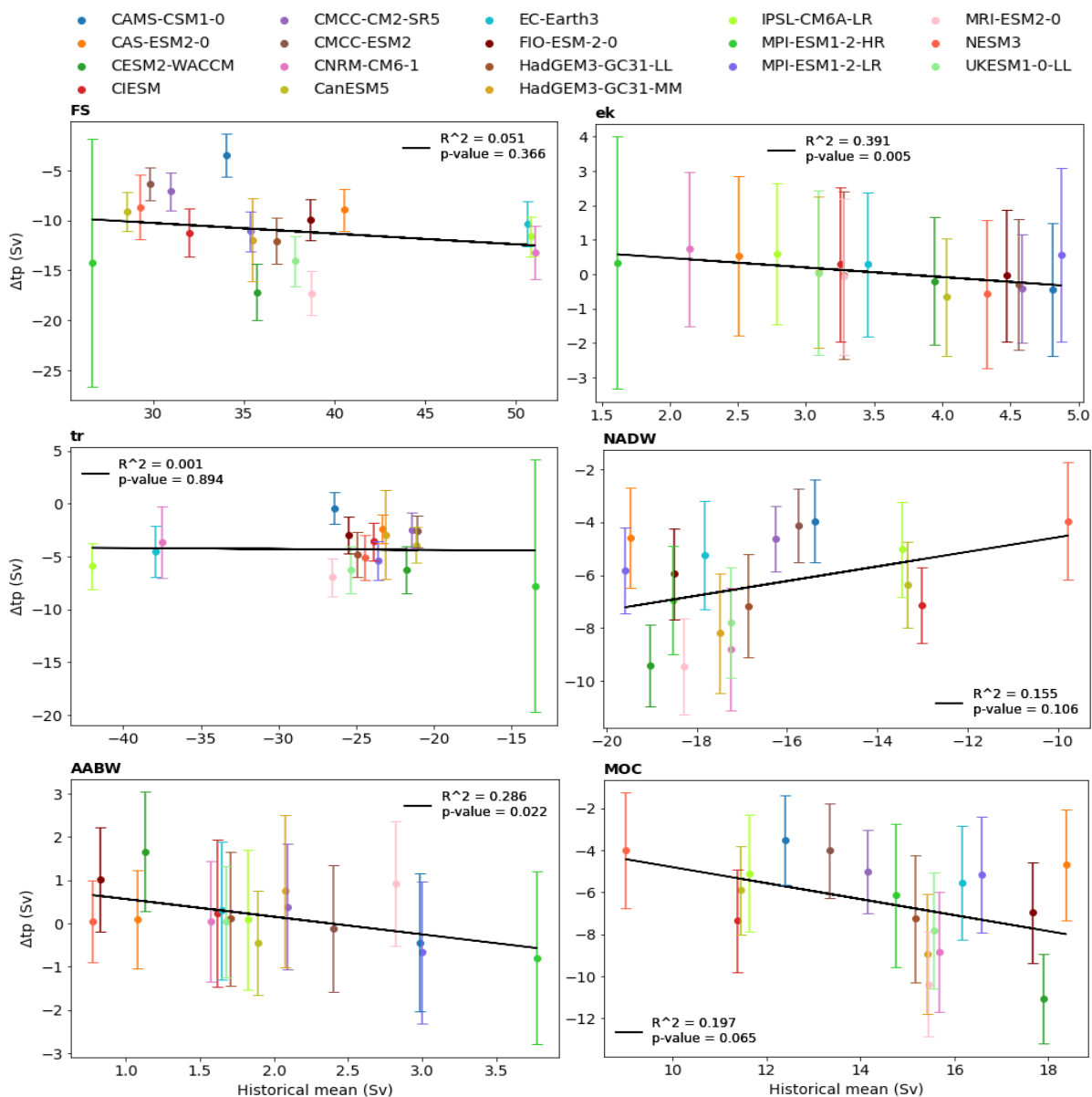


Figure 15: Change under SSP585 against historical mean for the different components. R^2 - and p -values are shown too.

5. Discussion

5.1 Historical period

5.1.1 *Strength of components*

A common feature among CMIP5 and CMIP6 models, which is observed in this study as well, is the tendency for the NADW cell to be too shallow compared to observational data (Wang et al., 2014; Weijer et al., 2020). All models analysed in this study were unable to correctly reproduce lower NADW transport at 26°N. Heuzé (2021) found that CMIP6 models do form lower NADW in the Greenland, Iceland and Norwegian (GIN) seas with properties similar to observations. However, none of the 35 models analysed in their study showed inter-basin spread of NADW beyond the Nordic Seas. Thus, models are unable to represent overflow of lower NADW across the Greenland-Iceland-Scotland ridge. This is caused by the small scale of overflow across this ridge, mainly through the Denmark Strait and the Faroe Bank Channel that are relatively narrow compared to the resolution of ocean models (Girton et al., 2006, Macrander et al., 2007). Additionally, excessive mixing of water related to flow over stepped topography occurs in models (Griffies et al., 2000). This results in lower NADW formed in the Nordic Seas to be transported southward as upper NADW. Additionally, models could compensate inadequate lower NADW overflow by increased upper NADW formation in the Labrador and Irminger Sea to obtain a more accurate AMOC strength (Heuzé, 2021). Even though the models analysed in this study show more upper NADW transport than RAPID estimates, we are unable to assess whether excessive mixing of lower NADW or compensation by increased upper NADW formation in other regions is the dominant cause.

The ensemble mean AMOC strength is lower than observed for the historical period, but models overestimate Florida Straits transport and thermocline recirculation. This overestimation is mainly caused by the inclusion of the Antilles Current in Florida Straits transport due to the absence of the Bahamas in most models, whereas RAPID data incorporates this current in upper mid-ocean transport. However, Meinen et al. (2019) found that the mean northward transport by the Antilles current from 2005 to 2015 equals 4.7 Sv. If we correct for this difference, Florida Straits transport and thermocline recirculation are still overestimated in models by 1.4 Sv and 2.9 Sv, respectively. The shallow NADW cell discussed above results in AABW transport over a larger depth interval, and thus an overestimation in models of this component. The inability to reproduce intermediate water at 26°N is likely related to increased mixing in the South Atlantic, causing a reduced northward extent of this water mass (Heuzé, 2021).

5.1.2 *Deep-water circulation*

The modelled strength of deep-water circulation varies greatly from RAPID estimates. Not only the absolute but also the relative strength of (re)circulation differs from observations, suggesting the driving mechanism of recirculation is the main cause of the discrepancy. Several studies have shown that the recirculation is predominantly driven by mesoscale eddies (Biló and Johns, 2020; Schulzki et al., 2021). The only model in our ensemble with an “eddy-present” resolution of 0.25° is HadGEM3-GC31-MM (Hewitt et al., 2020). This model represents deep-water recirculation more accurately than all other models (including HadGEM3-GC31-LL), with a DWBC of -23.9 Sv and interior transport of 6.4 Sv. Additionally, the width of the DWBC is much closer to observations (Figure 16). This supports the hypothesis that the disagreement between modelled and observed deep-water (re)circulation strength is caused by the use of eddy-parameterising instead of eddy-permitting models in this study.

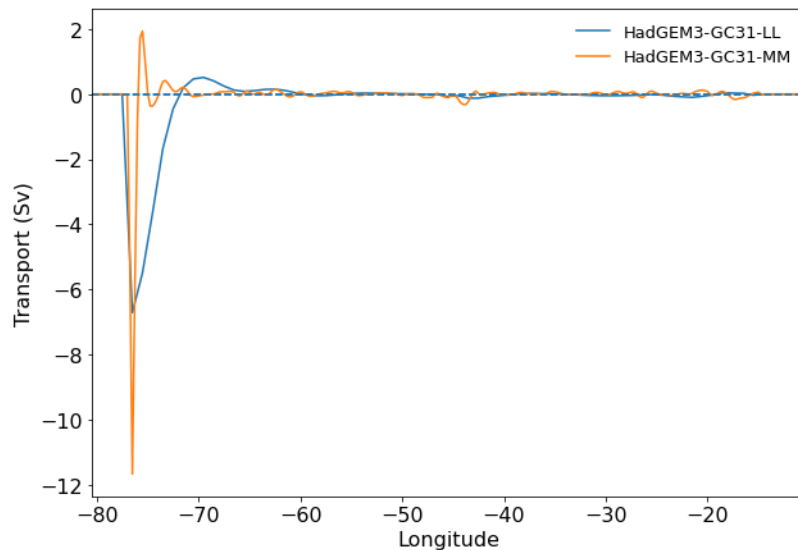


Figure 16: Vertically summed NADW transport of the low- and “high”-resolution HadGEM3-GC31 model for the historical period.

The historical view of NADW transport by a dominant DWBC has been challenged by several studies, which showed that southward transport of floats in the North Atlantic most often occurs via interior pathways rather than by a distinct DWBC (Fischer and Schott, 2002, Bower et al., 2009, Bower et al., 2019). Our results show that NADW transport in models is dominated by a DWBC, with only minor transport via interior pathways. Spence et al. (2012) found that the separation from the DWBC occurs when the viscosity in models is reduced. Thus, NADW transport in models imposing a high viscosity is dominated by a DWBC, while models with a reduced viscosity are able to reproduce NADW transport via interior pathways. None of the models analysed in this study included viscosity in their output data. Therefore, a review of the model papers is needed to get an indication of the viscosity used in each model, which is beyond the scope of this study. However, the viscosity is generally reduced in models with a higher resolution and the models analysed in this study have a relatively coarse resolution. This could indicate that the presence of a dominant DWBC in this study is indeed related to the viscosity of the models. Though, we do not find significant differences in southward interior transport between the low- and “high”-resolution HadGEM3-GC31 models (Figure 16), which stresses the necessity of viscosity data as conclusive evidence for this argument.

5.1.3 Variability of components

The total variability of the MOC is underestimated by all models, but Florida Straits transport, thermocline recirculation and Ekman transport show variabilities comparable to RAPID data for most models, with MPI-ESM1-2-HR as a clear outlier. It is expected that models with a higher resolution yield a higher variability (Roberts, 2020), but the variability values of Florida Straits transport and thermocline recirculation of this particular model are too divergent from other models. This might suggest that MPI-ESM1-2-HR is numerically unstable.

When decomposing the variability in three different components, it becomes clear that low-frequency and seasonal variability in models are dominated by Florida Straits transport and thermocline recirculation, even when MPI-ESM1-2-HR is excluded (Appendix H). In observational data, NADW and thermocline recirculation show the largest variability in these domains. As discussed above, models are not able to reproduce overflow of NADW across the Greenland-Iceland-Scotland Ridge. Therefore, northward flow through the Florida Straits is mostly balanced by southward flowing upper mid-ocean transport (i.e. tr) and less by deep-water transport (NADW). Thus variability of Florida Straits transport is correlated to thermocline recirculation in CMIP6 models. Since both

components have opposing transport directions, their variability is counterbalanced when obtaining the total MOC variability. Observations show a much lower variability in Florida Straits transport and this relatively stable northward flow is balanced by both thermocline recirculation and NADW transport, causing the latter two components to be correlated in the low-frequency domain (McCarthy et al., 2012). This modelled correlation between FS and tr in models is most likely driven by wind stress curl variability. Another factor that could play an important role here is topography. Due to the coarse resolution of the analysed models, the Bahamas are absent in most models. Therefore, impediment of the correlation between Florida Straits transport and thermocline recirculation by this island group is (largely) absent. Additionally, Meinen et al. (2019) showed that variability of the Antilles Current is correlated with thermocline recirculation, but no significant correlation was found between the Antilles Current and Florida Straits transport. Since the Antilles Current is included in Florida Straits transport in models, this most likely contributes significantly to the correlation with thermocline recirculation.

Other studies indicate that insufficient variability in wind forcing could play a significant role in underestimation of low-frequency variability of the MOC in models (Roberts et al., 2014, Yan et al., 2018). It is expected that this would be reflected in the variability of Ekman transport as it is driven by zonal wind stress. Our results show that the low-frequency variability of the Ekman component is somewhat lower than observed, but the difference with observations is relatively small. Additionally, the low-frequency variability of Florida Straits transport and thermocline recirculation, which are mainly driven by wind stress curl, should also be underestimated in this case (Zhao and Johns, 2014). As discussed above, the low-frequency variability of Florida Straits transport is largely overestimated by models due to the inclusion of the Antilles Current. The variability of Florida Straits transport and thermocline recirculation is expected to decrease when the Antilles Current is included in the latter component instead. Therefore, insufficient variability in wind forcing could have a significant effect on the underestimation of MOC variability in the low-frequency domain, but this cannot be concluded from our results.

The high-frequency variability is dominated by Ekman in models and by NADW in observations. Balan Sarojini et al. (2011) showed that the high-frequency variability of the AMOC is mainly set by the atmosphere in models. Therefore, it is not surprising that Ekman dominates this variability domain in CMIP6 models. It is still unknown what drives the high-frequency variability of NADW transport in RAPID data, but our results show that models are unable to reproduce this variability. This is likely related to the inability of models to reproduce lower NADW transport, but further research is needed to support this hypothesis.

5.2 SSP585

5.2.1 Contribution of components to AMOC decline

The future decline of the AMOC under SSP585 is in line with other modelling studies (Levang and Schmitt, 2020; Weijer et al, 2020; Roberts et al., 2020). The main cause of this decline are temperature dynamics. As high latitudes experience more warming due to increased greenhouse gas emissions than mid and low latitudes, the north-south pressure gradient decreases resulting in an AMOC decline (Fox-Kemper et al., 2021). Another contributor to changes in the AMOC is anthropogenic aerosol forcing. Several studies found significant AMOC strengthening as a result of increased anthropogenic aerosols in historical CMIP6 runs (e.g. Menary et al., 2020; Hassan et al., 2021). In contrast to greenhouse gases, an increase in aerosols has a cooling effect due to the increased reflection of short wave radiation, which results in a strengthening of the AMOC (Hassan et al., 2021). Similarly, part of the future decline could be related to a decrease in anthropogenic aerosol forcing (CMIP5: Ma et al., 2020). The effect of fresh water input due to Greenland ice sheet melting is not included in CMIP models, though it has been shown to affect weakening of the AMOC (Bakker et al., 2016). Interestingly, the rate of AMOC decline is similar for different emission scenarios until 2060. Only after 2060, different SSPs show divergent projections for several models (Weijer et al., 2020). It is hypothesised that the rate of AMOC decline is related to cumulative carbon emissions, so that only after 2060 differences in SSPs are significant compared to historical carbon emission (Herrington & Zickfeld, 2014; Steinacher and Joos, 2016).

As Ekman transport shows no significant change, the AMOC decline (-6.6 Sv) is the result of the difference in decline between Florida Straits transport (-11.0 Sv) and thermocline recirculation (4.4 Sv). This difference is balanced by a decrease in NADW transport (6.4 Sv) and a small increase in AABW (0.2 Sv), so that the net change through the cross section remains zero.

We identify three potential drivers of changes in the main components (i.e. FS, tr and NADW), which are changes in (1) wind stress curl, (2) NADW transport due to changes in convection and/or mixing and (3) input from the South Atlantic. The mechanisms of drivers (2) and (3) are relatively straightforward, but the effect of wind stress curl on meridional transport requires further explanation. As shown in the Method section, the wind stress curl is calculated by:

$$\text{curl } \tau = d\tau_y/dx - d\tau_x/dy$$

This wind stress curl causes either convergence or divergence in Ekman transport, since it acts perpendicular to the direction of the wind stress. The convergence or divergence result in downward or upward transport, respectively (Talley, 2011). This process is called Ekman pumping, and affects the density field of the ocean (Gill and Adrian, 1982). This causes meridional transport, as shown by the thermal wind balance:

$$\frac{dv}{dz} = \frac{g}{\rho f} \frac{d\rho}{dx}$$

Where g is the gravitational constant, ρ is the water density and f is the Coriolis parameter.

Additionally, Ekman pumping causes “squashing” (downward) or “stretching” (upward) of the water column beneath (Talley, 2011). This has implications for the potential vorticity (i.e. spin) of the water column, which is defined as:

$$Q = (\zeta + f)/H$$

Where ζ is the relative vorticity, f is the planetary vorticity and H is the height of the water column. Since potential vorticity is conserved, a decrease (“squashing”) or increase (“stretching”) of H is

balanced by a decrease or increase of either relative or planetary vorticity. Due to the small vorticity in the ocean interior (Talley, 2011), Ekman pumping is balanced by a decrease (equatorward transport) or increase (poleward transport) of planetary vorticity. This relationship between wind stress curl and meridional transport is shown by the Sverdrup balance:

$$V = \frac{\text{curl } \tau}{\rho\beta}$$

Where ρ is the water density and β is the change of Coriolis parameter f with latitude. In this study, we do not compute Sverdrup transport from wind stress curl, but merely use the explanation above to show that there is a linear relationship between wind stress curl and meridional transport.

Since the gyre circulation is driven by wind stress curl (DiNezio et al., 2009; Zhao and Johns, 2014), we expect a decrease of this driver to affect both Florida Straits transport and thermocline recirculation. A decline in NADW transport could be compensated by both a decrease in Florida Straits transport as well as an increase in thermocline recirculation. Similarly, a reduction of South Atlantic input (causing reduced FS transport) could be balanced by decreased NADW transport and thermocline recirculation.

In order to quantify changes in gyre circulation due to wind stress curl, we computed the mean curl along the 26°N section for the historical and SSP585 period. Note that the values are negative (i.e. clockwise rotation), which results in southward Sverdrup transport as explained above. The average wind stress curl shows high seasonal variability, but with a clear decreasing trend under SSP585 (Figure 17). With a magnitude of -14% compared to the historical period, the relative decline is very similar to the decrease in thermocline circulation of -17% over the same period (Figure 12). From this, we can conclude that the reduction of thermocline circulation (4.4 Sv) is almost entirely caused by a decline in wind stress curl. As mentioned above, we expect Florida straits transport to be affected by this decline as well. Therefore, a decrease in this component of $-11 + 4.4 = -6.6$ Sv is caused by drivers other than wind stress curl. Since changes in NADW formation can be communicated on short timescales by boundary waves (i.e. Kelvin waves), we are unable to indicate whether changes in NADW formation or South Atlantic input dominate the Florida Straits decline in models (Buckley and Marshall, 2016). To do so, decomposition of the AMOC into its components should be performed on several latitudes, both north and south of 26°N. From this, it could be examined whether the decline in Florida Straits transport leads the decline in NADW transport or vice versa. Due to mass balance, lagged regression between the MOC and transport components through our section did not yield any results.

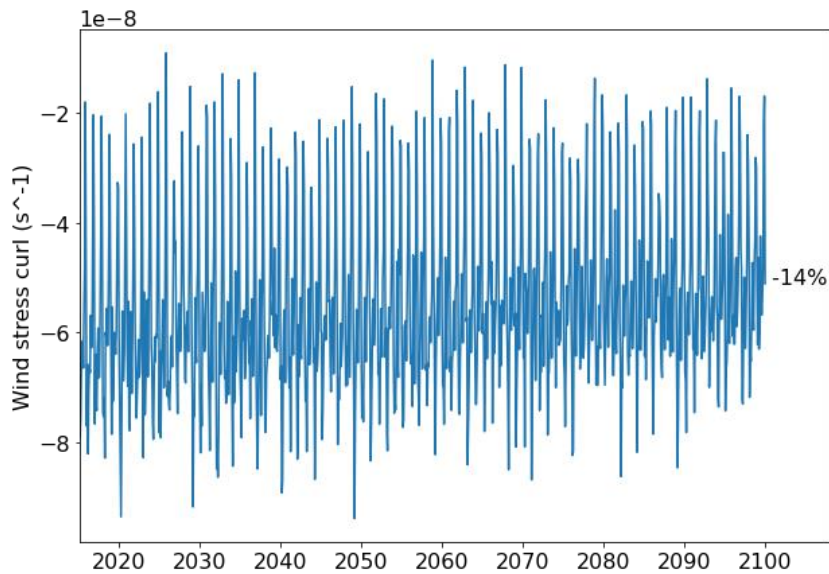


Figure 17: Timeseries of the ensemble mean wind stress curl under SSP585. The percentage shows the decline relative to the historical period.

Note that there is relatively more thermocline recirculation by the end of the 21st century. This affects the heat transport by the AMOC, since the difference in temperature between NADW and northward upper-ocean water is the cause of the large heat flux. An increase in the relative importance of thermocline recirculation would therefore result in a relative decrease of transported heat (Thomas et al., 2012).

5.2.2 Historical mean vs SSP585 future changes

Previous modelling studies showed a relationship between the mean state of the AMOC and its decline under different forcing scenarios, where models with a stronger mean state showed a larger decline (Gregory et al., 2005; Rugenstein et al., 2013; Weijer et al., 2020). From our analysis follows that models with a higher historical mean indeed show a larger future decline in Ekman transport ($p=0.005$), AABW ($p=0.022$) and total MOC ($p=0.065$). Though significant ($p < 0.1$), the relationships are all very weak. Weijer et al. (2020) found a much stronger relationship between the historical mean and future decline of the AMOC, with a significant r -value of -0.78 for SSP585. However, in their study multiple ensemble member per model are used and cluster analysis is performed to indicate outliers, which are excluded from the relationship. We do not see any basis for the exclusion of specific models in our study. Therefore, the relationships found in this study are not strong enough to be used as emergent constraints (Hall et al., 2019).

Nonetheless, it is interesting to discuss the physical cause of the relationship between historical mean state and sensitivity to increased carbon emissions. Levermann et al. (2007) argued that models with a lower historical mean MOC transport less heat to convection sites, resulting in farther southward extent of sea ice compared to models with a higher historical mean MOC. Atmospheric warming in future scenarios causes a larger retreat of sea ice for models with larger initial sea ice cover. This results in more oceanic heat loss, which stabilizes the decline in AMOC strength. To examine this mechanism in our model ensemble, we relate AMOC changes to northern hemisphere sea ice extent and seasonality. From the hypothesis of Levermann, we would expect that models with a larger historical sea ice extent or seasonality show a smaller future decline of the AMOC. We observe no relationship between historical sea ice extent and AMOC decline in our model ensemble (Figure 18). We find only a weak relationship between sea ice seasonality and future AMOC decline, which is not significant within the 90% confidence interval ($p=0.108$). However, this does not

necessarily invalidate the argument made by Levermann. Since we only find a weak relationship between the historical mean state and future change of the AMOC, we do not expect to find a strong relationship with the asserted mechanism causing this relationship. Additionally, model NESM3 is not included in the sea ice relationship, while this model affects the significance of the relationship between historical mean state and AMOC decline to a great extent (Figure 15). We were unable to compute the sea ice extent and seasonality, since the area of the sea ice grid cells was not included in the available dataset. Therefore, the area of each grid cell could not be computed. Finally, the sea ice extent and seasonality shown are for the area above 40°N, thus including sea ice cover in the Bering Sea. Changes in sea ice extent due to local factors in this area could affect the results shown here.

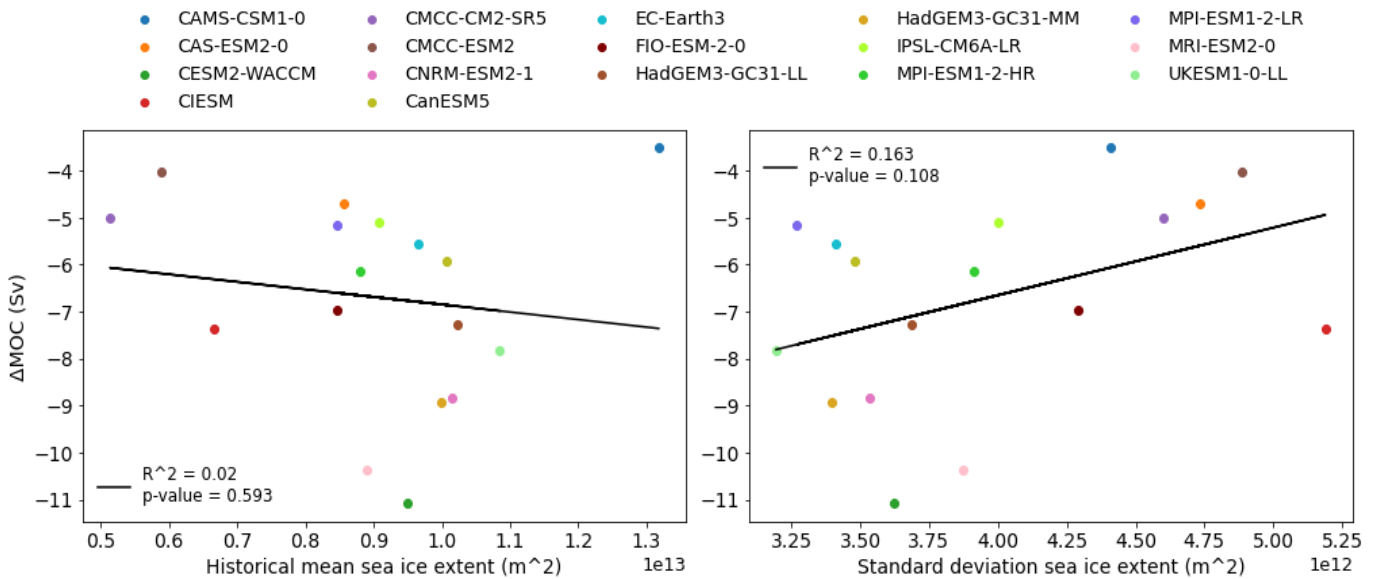


Figure 18: Change in AMOC strength under SSP585 against historical mean sea ice extent (left) and standard deviation of sea ice extent (right). R^2 - and p -values of the relationships are shown too.

Despite this, sea ice does not seem to extent to the primary regions of convection. In Figure 19, we show the minimum and maximum sea ice extent of the historical period for CMCC-ESM2, a model which shows a high seasonality and a low AMOC decline. The dominant regions of deep-water formation in CMIP6 models are shown in red, estimated from mixed layer depth data of Heuzé (2021). Since the convective regions are almost entirely ice-free during the time of maximum sea ice extent, we hypothesize that increased ocean heat loss due to melting of sea ice would only have a minor effect on the AMOC strength. Even though the mixed layer depth data is based on an ensemble mean in which CMCC-ESM2 is not included, none of the 35 models analysed by Heuzé (2021) show areas of deep convection extending further north than the boundaries drawn here. Thus, we find it appropriate to use these boundaries as a first indication the convective regions. A more detailed examination where mixed layer depths of every model are compared to sea ice extent during minima and maxima is beyond the scope of this study.

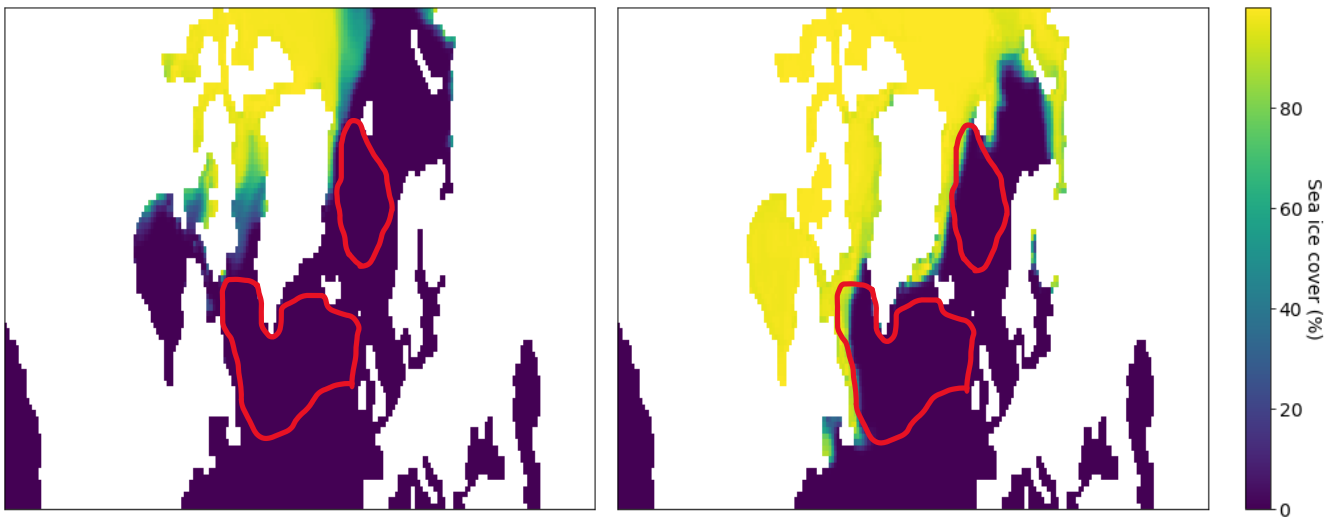


Figure 19: the minimum (left) and maximum(right) sea ice extent of the historical period for CMCC-ESM2. Red lines indicate the regions of deep-water formation in CMIP6 models, from Heuzé (2021).

5.3 Uncertainties

The uncertainties of CMIP6 models are best shown by their inter-model spread. In the Results section and Appendix E, this spread is quantified for both the historical and SSP585 period. Since it is crucial to keep these uncertainties in mind, we briefly discuss the inter-model spread again here. In Figure 20, the means of the different components are shown for the historical period (left) and for the SSP585 decline (right), with error bars indicating the inter-model spread. Note that the absolute historical mean values are displayed to improve the visualisation of the spread. This clearly shows the substantial differences between models, both in historical mean state and change under SSP585. As an example, consider the inter-model spread of the historical mean MOC. This spread is 9.4 Sv, with a minimum of 9 Sv (NESM3, -2.2σ where σ is the standard deviation of the model spread) and a maximum of 18.4 Sv (CAS-ESM2-0, $+1.5\sigma$). The standard deviation of the ensemble spread (2.5 Sv) is more than twice the standard deviation of the ensemble mean timeseries (1.2 Sv). For historical deep-water circulation, the standard deviation of inter-model spread is also relatively high (interior: 2.2 Sv, DWBC: 3.8 Sv), but closer to the variability of the ensemble mean timeseries (interior and DWBC: 2.9 Sv). Therefore, it is important to stress that our results are highly dependent on the models that are included in this study.

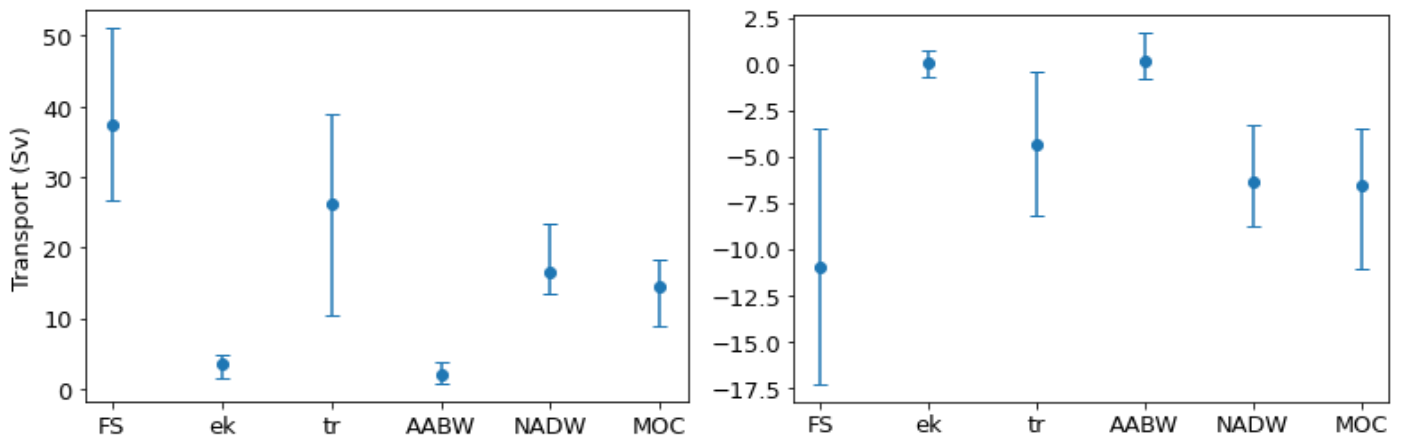


Figure 20: Historical mean (left) and decline under SSP585 (right) for each component. Error bars indicate the inter-model spread. Note that the absolute values of the historical mean are shown.

5.4 General remarks

The effect of increased model resolution on the representation of the AMOC in models is extensively studied, with contrasting results. Some studies find no clear effect of model resolution on mechanisms affecting the AMOC (Winton et al., 2014; Weijer et al., 2020; Heuzé, 2021), others find positive (e.g. Marzocchi et al., 2015; Danek et al., 2019) or negative effects (e.g. Koenigk et al., 2020). Generally, the effect of model resolution on AMOC strength and sensitivity seems to be model-dependent (Fox-Kemper et al., 2021). In this study, only two models with a low- and “high”-resolution variant are included, where the “high”-resolution variant of these models is still relatively coarse compared to the resolution of, for example, HadGEM3-GC31-HH of $1/12^\circ$. The AMOC of HadGEM3-GC31-MM (MPI-ESM1-2-HR) has a higher (lower) historical mean, a lower (higher) total variability, a stronger (weaker) DWBC and a larger (larger) future decline than its low-resolution variant. However, only the difference in variability of the MPI-ESM1-2 models and in DWBC of the HadGEM3-GC31 models is large. Therefore, we conclude that there is no coherent effect of increased horizontal resolution on the representation of the AMOC in these models. Note that the resolution of MPI-ESM1-2-HR is still too coarse to be eddy-permitting.

There are other factors that could improve the AMOC representation in CMIP6 models. For example, the use of overflow parameterization over the Greenland-Iceland-Scotland Ridge could increase lower NADW transport to the subtropical region (Briegleb et al., 2010; Gent et al., 2011). Additionally, it has been shown that changes in the AMOC are related to modelled stratosphere variability due to troposphere coupling (Reichler et al., 2012; Manzini et al., 2012). Haase et al. (2018) pointed out that a more accurate representation of the stratosphere could improve the overturning circulation in models.

Even though a lot of emphasis has been put on documentation and model output requirements in CMIP Phase 6, there is still room for improvement. Generalising the inclusion of the overturning stream function in the model output data would enable us to review the calculated stream function of all models. Additionally, we did not analyse the SSP585 run of CNRM-ESM2-1, since temperature data of this model is not included for the SSP585 period. Similarly, NESM3 is excluded from the sea ice analysis, since data on the grid cell area was not submitted. Finally, a more straightforward way to obtain viscosity data could have allowed for an analysis of the effect of viscosity on NADW transport via interior pathways.

For future research, we recommend to use the same definition for Florida Straits transport and thermocline recirculation in RAPID and CMIP6 data. Since most CMIP6 models have a coarse resolution, the Bahamas are not present. Therefore, we could not divide western boundary transport into the Gulf Stream and Antilles Current. Thus, to overcome this mismatch, we advise to include RAPID measurements of the Antilles Current in Florida Straits transport when comparing it to modelled transport components. Furthermore, modelling studies on the different transport components at several latitudes could provide valuable insight into the leading drivers of AMOC changes. Weijer et al. (2020) did compare the representation of the AMOC in CMIP6 models with both RAPID (26°N) and SAMBA (34°S) observations, but studies on the modelled AMOC north of 26°N are lacking. Since most studies have focussed on interannual to decadal variability of the AMOC and NADW transport, we would like to stress the relevance of additional research on high-frequency NADW variability. NADW dominates high-frequency variability in RAPID data and variability is generally largest on this timescale.

6. Conclusion

In this study, we examined the ability of CMIP6 models to reproduce the strength and variability of the different transport components of the AMOC, as measured by the RAPID array. The variability was decomposed into low-frequency, seasonal and high-frequency variability. Additionally, the modelled deep-water circulation was analysed for the historical period. We also examined future changes in the strength of the components and deep-water circulation under SSP585 and related these changes to the historical mean state of each component.

For the historical period (2004-2014), we found that the underestimation of the total AMOC strength is caused by reduced transport of lower NADW over the Greenland-Iceland-Scotland Ridge, due to the small scale of overflow compared to the resolution of models and increased mixing at the Ridge. This is compensated by increased recirculation in the subtropical gyre and results in more AABW transport in models. Deep-water circulation in models is dominated by a distinct DWBC with minor interior recirculation compared to observations, which is likely related to model resolution. We show that the low-frequency variability of Florida Straits transport is largely overestimated and hypothesize that the inclusion of the Antilles Current in this component in models is a significant contributor to this discrepancy. The variability of NADW is underestimated, most likely due to the inability of models to reproduce lower NADW overflow.

For the SSP585 period (2015-2100), we find a decline in the Florida Straits transport, thermocline recirculation and NADW transport. Decreased thermocline recirculation is related to a decline in wind stress curl along the section. Therefore, the future decline in the AMOC is likely caused by decreased Florida Straits transport, either due to reduced input from the South Atlantic or communication of reduced NADW transport by boundary waves. We find significant relationships ($p < 0.01$) between the historical mean state and future changes of the total AMOC, Ekman and AABW transport. However, these relationships are too weak to be used as “emergent constraints”. Additionally, the relationship cannot be explained by sea ice extent or seasonality in this study.

Our results give insight into the cause of disagreement in the modelled and observed AMOC. For future research, we advise to include RAPID measurements of the Antilles Current in Florida Straits transport when comparing it to modelled transport components. Furthermore, similar studies at several latitudes, especially north of 26°N , could provide valuable insight into the leading drivers of AMOC changes. Since most studies have focussed on interannual to decadal variability of the AMOC and NADW transport, we emphasize the relevance of additional research on high-frequency NADW variability.

Acknowledgements

I acknowledge the UK Natural Environment Research Council and US National Science Foundation for funding the RAPID-MOCHA project and making the data freely available. The CMIP6 project is coordinated by the World Climate Research Programme and the data shared by the different modelling groups is made available by the Centre for Environmental Data Analysis. I would like to thank Wilco Hazeleger and Sybren Drijfhout for the meetings and feedback during this research project. Additionally, I would like to thank Jennifer Mecking for her help with the Python scripts and sharing the model mask files. Lastly, I would like to thank Harry Bryden for the interesting discussion on the results.

Code availability

The code used to obtain the results of this study and a file containing metadata of the models is freely available on GitHub: https://github.com/jordibeunk/MSc_Thesis.git

References

- Bakker, P., Schmittner, A., Lenaerts, J. T. M., Abe-Ouchi, A., Bi, D., van den Broeke, M. R., ... & Yin, J. (2016). Fate of the Atlantic Meridional Overturning Circulation: Strong decline under continued warming and Greenland melting. *Geophysical Research Letters*, *43*(23), 12-252.
- Balan Sarojini, B., Gregory, J. M., Tailleux, R., Bigg, G. R., Blaker, A. T., Cameron, D. R., ... & Sinha, B. (2011). High-frequency variability of the Atlantic meridional overturning circulation. *Ocean Science*, *7*(4), 471-486.
- Biastoch, A., Böning, C. W., Getzlaff, J., Molines, J. M., & Madec, G. (2008). Causes of interannual–decadal variability in the meridional overturning circulation of the midlatitude North Atlantic Ocean. *Journal of climate*, *21*(24), 6599-6615.
- Biló, T. C., & Johns, W. E. (2020). The deep western boundary current and adjacent interior circulation at 24°–30° N: Mean structure and mesoscale variability. *Journal of Physical Oceanography*, *50*(9), 2735-2758.
- Boucher, Olivier; Denvil, Sébastien; Levavasseur, Guillaume; Cozic, Anne; Caubel, Arnaud; Foujols, Marie-Alice; Meurdesoif, Yann; Balkanski, Yves; Checa-Garcia, Ramiro; Hauglustaine, Didier; Bekki, Slimane; Marchand, Marion (2021). IPSL CM6A-LR-INCA model output prepared for CMIP6 CMIP historical. Version 20211003. Earth System Grid Federation. <https://doi.org/10.22033/ESGF/CMIP6.13601>
- Boucher, Olivier; Denvil, Sébastien; Levavasseur, Guillaume; Cozic, Anne; Caubel, Arnaud; Foujols, Marie-Alice; Meurdesoif, Yann; Cadule, Patricia; Devilliers, Marion; Dupont, Elliott; Lurton, Thibaut (2019). IPSL CM6A-LR model output prepared for CMIP6 ScenarioMIP ssp585. Version 20211003. Earth System Grid Federation. <https://doi.org/10.22033/ESGF/CMIP6.5271>
- Bower, A. S., Lozier, M. S., Gary, S. F., & Böning, C. W. (2009). Interior pathways of the North Atlantic meridional overturning circulation. *Nature*, *459*(7244), 243-247.
- Bower, A., Lozier, S., Biastoch, A., Drouin, K., Foukal, N., Furey, H., ... & Zou, S. (2019). Lagrangian views of the pathways of the Atlantic Meridional Overturning Circulation. *Journal of Geophysical Research: Oceans*, *124*(8), 5313-5335.
- Briegleb, B. P., Danabasoglu, G., & Large, W. G. (2010). An Overflow parameterization for the ocean component of the Community Climate System Model (No. NCAR/TN-481+STR). *University Corporation for Atmospheric Research*.
- Bryden, H. L. (2021). Wind-driven and buoyancy-driven circulation in the subtropical North Atlantic Ocean. *Proceedings of the Royal Society A*, *477*(2256), 20210172.
- Bryden, H. L., Mujahid, A., Cunningham, S. A., & Kanzow, T. (2009). Adjustment of the basin-scale circulation at 26° N to variations in Gulf Stream, deep western boundary current and Ekman transports as observed by the RAPID array. *Ocean Science*, *5*(4), 421-433.
- Buckley, M. W., & Marshall, J. (2016). Observations, inferences, and mechanisms of the Atlantic Meridional Overturning Circulation: A review. *Reviews of Geophysics*, *54*(1), 5-63.
- Cao, Jian (2019). NUIST NESMv3 model output prepared for CMIP6 ScenarioMIP ssp585. Version 20211003. Earth System Grid Federation. <https://doi.org/10.22033/ESGF/CMIP6.8790>

- Cao, Jian; Wang, Bin (2019). NUIST NESMv3 model output prepared for CMIP6 CMIP historical. Version 20211003. Earth System Grid Federation. <https://doi.org/10.22033/ESGF/CMIP6.8769>
- Chai, Zhaoyang (2020). CAS CAS-ESM1.0 model output prepared for CMIP6 CMIP historical. Version 20211003. Earth System Grid Federation. <https://doi.org/10.22033/ESGF/CMIP6.3353>
- Unkown (2018). CAS CAS-ESM1.0 model output prepared for CMIP6 ScenarioMIP ssp585. Earth System Grid Federation. <http://cera-www.dkrz.de/WDCC/meta/CMIP6/CMIP6.ScenarioMIP.CAS.CAS-ESM2-0.ssp585>
- Cheng, W., Bitz, C. M., & Chiang, J. C. (2007). Adjustment of the global climate to an abrupt slowdown of the Atlantic meridional overturning circulation. *Geophysical Monograph-American Geophysical Union*, 173, 295.
- Danabasoglu, Gokhan (2019). NCAR CESM2-WACCM model output prepared for CMIP6 ScenarioMIP ssp585. Version 20211003. Earth System Grid Federation. <https://doi.org/10.22033/ESGF/CMIP6.10115>
- Danabasoglu, Gokhan (2019). NCAR CESM2-WACCM-FV2 model output prepared for CMIP6 CMIP historical. Version 20211003. Earth System Grid Federation. <https://doi.org/10.22033/ESGF/CMIP6.11298>
- Danek, C., Scholz, P., & Lohmann, G. (2019). Effects of high resolution and spinup time on modeled North Atlantic circulation. *Journal of Physical Oceanography*, 49(5), 1159-1181.
- Dengler, M., Schott, F. A., Eden, C., Brandt, P., Fischer, J., & Zantopp, R. J. (2004). Break-up of the Atlantic deep western boundary current into eddies at 8 S. *Nature*, 432(7020), 1018-1020.
- DiNezio, P. N., Gramer, L. J., Johns, W. E., Meinen, C. S., & Baringer, M. O. (2009). Observed interannual variability of the Florida Current: Wind forcing and the North Atlantic Oscillation. *Journal of Physical Oceanography*, 39(3), 721-736.
- EC-Earth Consortium (EC-Earth) (2019). EC-Earth-Consortium EC-Earth3 model output prepared for CMIP6 ScenarioMIP ssp585. Version 20211003. Earth System Grid Federation. <https://doi.org/10.22033/ESGF/CMIP6.4912>
- EC-Earth Consortium (EC-Earth) (2021). EC-Earth-Consortium EC-Earth-3-CC model output prepared for CMIP6 CMIP historical. Version 20211003. Earth System Grid Federation. <https://doi.org/10.22033/ESGF/CMIP6.4702>
- Eyring, V., Bony, S., Meehl, G. A., Senior, C. A., Stevens, B., Stouffer, R. J., & Taylor, K. E. (2016). Overview of the Coupled Model Intercomparison Project Phase 6 (CMIP6) experimental design and organization. *Geoscientific Model Development*, 9(5), 1937-1958.
- Fischer, J., & Schott, F. A. (2002). Labrador Sea Water tracked by profiling floats—From the boundary current into the open North Atlantic. *Journal of Physical Oceanography*, 32(2), 573-584.
- Fontela, M., García-Ibáñez, M. I., Hansell, D. A., Mercier, H., & Pérez, F. F. (2016). Dissolved organic carbon in the North Atlantic meridional overturning circulation. *Scientific reports*, 6(1), 1-9.
- Fox-Kemper, B., H. T. Hewitt, C. Xiao, G. Aðalgeirsdóttir, S. S. Drijfhout, T. L. Edwards, N. R. Golledge, M. Hemer, R. E. Kopp, G. Krinner, A. Mix, D. Notz, S. Nowicki, I. S. Nurhati, L. Ruiz, J-B. Sallée, A. B. A. Slangen, Y. Yu, 2021, Ocean, Cryosphere and Sea Level Change. In: *Climate Change 2021: The Physical*

- Science Basis. Contribution of Working Group I to the Sixth Assessment Report of the Intergovernmental Panel on Climate Change* [Masson-Delmotte, V., P. Zhai, A. Pirani, S. L. Connors, C. Péan, S. Berger, N. Caud, Y. Chen, L. Goldfarb, M. I. Gomis, M. Huang, K. Leitzell, E. Lonnoy, J.B.R. Matthews, T. K. Maycock, T. Waterfield, O. Yelekçi, R. Yu and B. Zhou (eds.)]. Cambridge University Press. In Press
- Frajka-Williams, E., Cunningham, S. A., Bryden, H., & King, B. A. (2011). Variability of Antarctic bottom water at 24.5° N in the Atlantic. *Journal of Geophysical Research: Oceans*, 116(C11).
- Frajka-Williams, E., Moat, B., Smeed, D., Rayner, D., Johns, W. E., Baringer, M. O., ... & Collins, J. (2021). RAPID-MOC time series April 2004 to March 2020 (v2020.1).
- Ganachaud, A. (2003). Large-scale mass transports, water mass formation, and diffusivities estimated from World Ocean Circulation Experiment (WOCE) hydrographic data. *Journal of Geophysical Research: Oceans*, 108(C7).
- Gent, P. R., Danabasoglu, G., Donner, L. J., Holland, M. M., Hunke, E. C., Jayne, S. R., ... & Zhang, M. (2011). The community climate system model version 4. *Journal of climate*, 24(19), 4973-4991.
- Gill, A. E., & Adrian, E. (1982). *Atmosphere-ocean dynamics* (Vol. 30). Academic press.
- Girton, J. B., Pratt, L. J., Sutherland, D. A., & Price, J. F. (2006). Is the Faroe Bank Channel overflow hydraulically controlled?. *Journal of Physical Oceanography*, 36(12), 2340-2349.
- Good, Peter (2020). MOHC HadGEM3-GC31-LL model output prepared for CMIP6 ScenarioMIP ssp585. Version 20211003. Earth System Grid Federation. <https://doi.org/10.22033/ESGF/CMIP6.10901>
- Good, Peter; Sellar, Alistair; Tang, Yongming; Rumbold, Steve; Ellis, Rich; Kelley, Douglas; Kuhlbrodt, Till (2019). MOHC UKESM1.0-LL model output prepared for CMIP6 ScenarioMIP ssp585. Version 20211003. Earth System Grid Federation. <https://doi.org/10.22033/ESGF/CMIP6.6405>
- Gregory, J. M., Dixon, K. W., Stouffer, R. J., Weaver, A. J., Driesschaert, E., Eby, M., ... & Thorpe, R. B. (2005). A model intercomparison of changes in the Atlantic thermohaline circulation in response to increasing atmospheric CO₂ concentration. *Geophysical Research Letters*, 32(12).
- Griffies, S. M., Böning, C., Bryan, F. O., Chassignet, E. P., Gerdes, R., Hasumi, H., ... & Webb, D. (2000). Developments in ocean climate modelling. *Ocean Modelling*, 2(3-4), 123-192.
- Haase, S., Matthes, K., Latif, M., & Omrani, N. E. (2018). The importance of a properly represented stratosphere for northern hemisphere surface variability in the atmosphere and the ocean. *Journal of Climate*, 31(20), 8481-8497.
- Haine, T., Böning, C., Brandt, P., Fischer, J., Funk, A., Kieke, D., ... & Visbeck, M. (2008). North Atlantic deep water formation in the Labrador Sea, recirculation through the subpolar gyre, and discharge to the subtropics. In *Arctic–Subarctic Ocean Fluxes* (pp. 653-701). Springer, Dordrecht.
- Hall, A., Cox, P., Huntingford, C., & Klein, S. (2019). Progressing emergent constraints on future climate change. *Nature Climate Change*, 9(4), 269-278.
- Hall, M. M., & Bryden, H. L. (1982). Direct estimates and mechanisms of ocean heat transport. *Deep Sea Research Part A. Oceanographic Research Papers*, 29(3), 339-359.
- Hassan, T., Allen, R. J., Liu, W., & Randles, C. A. (2021). Anthropogenic aerosol forcing of the Atlantic meridional overturning circulation and the associated mechanisms in CMIP6 models. *Atmospheric Chemistry and Physics*, 21(8), 5821-5846.

Herrington, T., & Zickfeld, K. (2014). Path independence of climate and carbon cycle response over a broad range of cumulative carbon emissions. *Earth System Dynamics*, 5(2), 409-422.

Heuzé, C. (2021). Antarctic bottom water and North Atlantic deep water in cmip6 models. *Ocean Science*, 17(1), 59-90.

Hewitt, H. T., Roberts, M., Mathiot, P., Biastoch, A., Blockley, E., Chassignet, E. P., ... & Zhang, Q. (2020). Resolving and parameterising the ocean mesoscale in earth system models. *Current Climate Change Reports*, 6(4), 137-152.

Huang, Wenyu (2019). THU CIESM model output prepared for CMIP6 CMIP historical. Version 20211003. Earth System Grid Federation. <https://doi.org/10.22033/ESGF/CMIP6.8843>

Huang, Wenyu (2020). THU CIESM model output prepared for CMIP6 ScenarioMIP ssp585. Version 20211003. Earth System Grid Federation. <https://doi.org/10.22033/ESGF/CMIP6.8863>

Jackson, L. C., Kahana, R., Graham, T., Ringer, M. A., Woollings, T., Mecking, J. V., & Wood, R. A. (2015). Global and European climate impacts of a slowdown of the AMOC in a high resolution GCM. *Climate dynamics*, 45(11), 3299-3316.

Johnson, H. L., Cessi, P., Marshall, D. P., Schloesser, F., & Spall, M. A. (2019). Recent contributions of theory to our understanding of the Atlantic meridional overturning circulation. *Journal of Geophysical Research: Oceans*, 124(8), 5376-5399.

Joyce, T. M., & Zhang, R. (2010). On the path of the Gulf Stream and the Atlantic meridional overturning circulation. *Journal of Climate*, 23(11), 3146-3154.

Jungclaus, Johann; Bittner, Matthias; Wieners, Karl-Hermann; Wachsmann, Fabian; Schupfner, Martin; Legutke, Stephanie; Giorgetta, Marco; Reick, Christian; Gayler, Veronika; Haak, Helmuth; de Vrese, Philipp; Raddatz, Thomas; Esch, Monika; Mauritsen, Thorsten; von Storch, Jin-Song; Behrens, Jörg; Brovkin, Victor; Claussen, Martin; Crueger, Traute; Fast, Irina; Fiedler, Stephanie; Hagemann, Stefan; Hohenegger, Cathy; Jahns, Thomas; Kloster, Silvia; Kinne, Stefan; Lasslop, Gitta; Kornblueh, Luis; Marotzke, Jochem; Matei, Daniela; Meraner, Katharina; Mikolajewicz, Uwe; Modali, Kameswarrao; Müller, Wolfgang; Nabel, Julia; Notz, Dirk; Peters-von Gehlen, Karsten; Pincus, Robert; Pohlmann, Holger; Pongratz, Julia; Rast, Sebastian; Schmidt, Hauke; Schnur, Reiner; Schulzweida, Uwe; Six, Katharina; Stevens, Bjorn; Voigt, Aiko; Roeckner, Erich (2019). MPI-M MPI-ESM1.2-HR model output prepared for CMIP6 CMIP historical. Version 20211003. Earth System Grid Federation. <https://doi.org/10.22033/ESGF/CMIP6.6594>

Koenigk, T., Fuentes-Franco, R., Meccia, V., Gutjahr, O., Jackson, L. C., New, A. L., ... & Sein, D. V. (2020). Deep water formation in the North Atlantic Ocean in high resolution global coupled climate models. *Ocean Science Discussions*, 1-39.

Kriegler, E., Bauer, N., Popp, A., Humpenöder, F., Leimbach, M., Strefler, J., ... & Edenhofer, O. (2017). Fossil-fueled development (SSP5): an energy and resource intensive scenario for the 21st century. *Global environmental change*, 42, 297-315.

Lee, J. Y., Marotzke, J., Bala, G., Cao, L., Corti, S., Dunne, J. P., ... & Zappa, G. (2021). Future global climate: scenario-based projections and near-term information. IPCC.

Levang, S. J., & Schmitt, R. W. (2020). What Causes the AMOC to Weaken in CMIP5?. *Journal of Climate*, 33(4), 1535-1545.

- Levermann, A., Mignot, J., Nawrath, S., & Rahmstorf, S. (2007). The role of northern sea ice cover for the weakening of the thermohaline circulation under global warming. *Journal of Climate*, 20(16), 4160-4171.
- Lovato, Tomas; Peano, Daniele (2020). CMCC CMCC-CM2-SR5 model output prepared for CMIP6 CMIP historical. Version 20211003. Earth System Grid Federation.
<https://doi.org/10.22033/ESGF/CMIP6.3825>
- Lovato, Tomas; Peano, Daniele (2020). CMCC CMCC-CM2-SR5 model output prepared for CMIP6 ScenarioMIP ssp585. Version 20211003. Earth System Grid Federation.
<https://doi.org/10.22033/ESGF/CMIP6.3896>
- Lovato, Tomas; Peano, Daniele; Butenschön, Momme (2021). CMCC CMCC-ESM2 model output prepared for CMIP6 CMIP historical. Version 20211003. Earth System Grid Federation.
<https://doi.org/10.22033/ESGF/CMIP6.13195>
- Lovato, Tomas; Peano, Daniele; Butenschön, Momme (2021). CMCC CMCC-ESM2 model output prepared for CMIP6 ScenarioMIP ssp585. Version 20211003. Earth System Grid Federation.
<https://doi.org/10.22033/ESGF/CMIP6.13259>
- Lozier, M. S. (2010). Deconstructing the conveyor belt. *science*, 328(5985), 1507-1511.
- Lozier, M. S., Li, F., Bacon, S., Bahr, F., Bower, A. S., Cunningham, S. A., ... & Zhao, J. (2019). A sea change in our view of overturning in the subpolar North Atlantic. *Science*, 363(6426), 516-521.
- Ma, X., Liu, W., Allen, R. J., Huang, G., & Li, X. (2020). Dependence of regional ocean heat uptake on anthropogenic warming scenarios. *Science advances*, 6(45), eabc0303.
- Macrander, A., Käse, R. H., Send, U., Valdimarsson, H., & Jónsson, S. (2007). Spatial and temporal structure of the Denmark Strait Overflow revealed by acoustic observations. *Ocean Dynamics*, 57(2), 75-89.
- Mahajan, S., Zhang, R., & Delworth, T. L. (2011). Impact of the Atlantic meridional overturning circulation (AMOC) on Arctic surface air temperature and sea ice variability. *Journal of Climate*, 24(24), 6573-6581.
- Manzini, E., Cagnazzo, C., Fogli, P. G., Bellucci, A., & Müller, W. A. (2012). Stratosphere-troposphere coupling at inter-decadal time scales: Implications for the North Atlantic Ocean. *Geophysical Research Letters*, 39(5).
- Marshall, J., & Speer, K. (2012). Closure of the meridional overturning circulation through Southern Ocean upwelling. *Nature Geoscience*, 5(3), 171-180.
- Marzocchi, A., Hirschi, J. J. M., Holliday, N. P., Cunningham, S. A., Blaker, A. T., & Coward, A. C. (2015). The North Atlantic subpolar circulation in an eddy-resolving global ocean model. *Journal of Marine Systems*, 142, 126-143.
- McCarthy, G. D., Smeed, D. A., Johns, W. E., Frajka-Williams, E., Moat, B. I., Rayner, D., ... & Bryden, H. L. (2015). Measuring the Atlantic meridional overturning circulation at 26 N. *Progress in Oceanography*, 130, 91-111.
- McCarthy, G., Frajka-Williams, E., Johns, W. E., Baringer, M. O., Meinen, C. S., Bryden, H. L., ... & Cunningham, S. A. (2012). Observed interannual variability of the Atlantic meridional overturning circulation at 26.5 N. *Geophysical Research Letters*, 39(19).

- Meinen, C. S., Johns, W. E., Moat, B. I., Smith, R. H., Johns, E. M., Rayner, D., ... & Garzoli, S. L. (2019). Structure and variability of the Antilles Current at 26.5 N. *Journal of Geophysical Research: Oceans*, 124(6), 3700-3723.
- Menary, M. B., Robson, J., Allan, R. P., Booth, B. B., Cassou, C., Gastineau, G., ... & Zhang, R. (2020). Aerosol-forced AMOC changes in CMIP6 historical simulations. *Geophysical Research Letters*, 47(14), e2020GL088166.
- Morey, S., Koch, M., Liu, Y., & Lee, S. K. (2017). Florida's oceans and marine habitats in a changing climate. *Florida's climate: Changes, variations, & impacts*.
- O'Neill, B. C., Kriegler, E., Riahi, K., Ebi, K. L., Hallegatte, S., Carter, T. R., ... & van Vuuren, D. P. (2014). A new scenario framework for climate change research: the concept of shared socioeconomic pathways. *Climatic change*, 122(3), 387-400.
- O'Neill, B. C., Tebaldi, C., Van Vuuren, D. P., Eyring, V., Friedlingstein, P., Hurtt, G., ... & Sanderson, B. M. (2016). The scenario model intercomparison project (ScenarioMIP) for CMIP6. *Geoscientific Model Development*, 9(9), 3461-3482.
- Rao, S., Klimont, Z., Smith, S. J., Van Dingenen, R., Dentener, F., Bouwman, L., ... & Tavoni, M. (2017). Future air pollution in the Shared Socio-economic Pathways. *Global Environmental Change*, 42, 346-358.
- Rayner, D., Hirschi, J. J. M., Kanzow, T., Johns, W. E., Wright, P. G., Frajka-Williams, E., ... & Cunningham, S. A. (2011). Monitoring the Atlantic meridional overturning circulation. *Deep Sea Research Part II: Topical Studies in Oceanography*, 58(17-18), 1744-1753.
- Reichler, T., Kim, J., Manzini, E., & Kröger, J. (2012). A stratospheric connection to Atlantic climate variability. *Nature Geoscience*, 5(11), 783-787.
- Ridley, Jeff; Menary, Matthew; Kuhlbrodt, Till; Andrews, Martin; Andrews, Tim (2019). MOHC HadGEM3-GC31-LL model output prepared for CMIP6 CMIP historical. Version 20211003. Earth System Grid Federation. <https://doi.org/10.22033/ESGF/CMIP6.6109>
- Ridley, Jeff; Menary, Matthew; Kuhlbrodt, Till; Andrews, Martin; Andrews, Tim (2019). MOHC HadGEM3-GC31-MM model output prepared for CMIP6 CMIP historical. Version 20211003. Earth System Grid Federation. <https://doi.org/10.22033/ESGF/CMIP6.6112>
- Ridley, Jeff; Menary, Matthew; Kuhlbrodt, Till; Andrews, Martin; Andrews, Tim (2019). MOHC HadGEM3-GC31-MM model output prepared for CMIP6 CMIP historical. Version 20211003. Earth System Grid Federation. <https://doi.org/10.22033/ESGF/CMIP6.6112>
- Roberts, C. D., Jackson, L., & McNeall, D. (2014). Is the 2004–2012 reduction of the Atlantic meridional overturning circulation significant?. *Geophysical Research Letters*, 41(9), 3204-3210.
- Roberts, M. J., Jackson, L. C., Roberts, C. D., Meccia, V., Docquier, D., Koenigk, T., ... & Wu, L. (2020). Sensitivity of the Atlantic meridional overturning circulation to model resolution in CMIP6 HighResMIP simulations and implications for future changes. *Journal of Advances in Modeling Earth Systems*, 12(8), e2019MS002014.
- Rong, Xinyao (2019). CAMS CAMS_CSM1.0 model output prepared for CMIP6 CMIP historical. Version 20211003. Earth System Grid Federation. <https://doi.org/10.22033/ESGF/CMIP6.9754>

- Rong, Xinyao (2019). CAMS CAMS-CSM1.0 model output prepared for CMIP6 ScenarioMIP ssp585. Version 20211003. Earth System Grid Federation. <https://doi.org/10.22033/ESGF/CMIP6.11052>
- Rossby, T. (1996). The North Atlantic Current and surrounding waters: At the crossroads. *Reviews of Geophysics*, 34(4), 463-481.
- Rugenstein, M. A., Winton, M., Stouffer, R. J., Griffies, S. M., & Hallberg, R. (2013). Northern high-latitude heat budget decomposition and transient warming. *Journal of climate*, 26(2), 609-621.
- Schulzki, T., Getzlaff, K., & Biastoch, A. (2021). On the Variability of the DWBC Transport Between 26.5° N and 16° N in an Eddy-Rich Ocean Model. *Journal of Geophysical Research: Oceans*, 126(6), Art-Nr.
- Schupfner, Martin; Wieners, Karl-Hermann; Wachsmann, Fabian; Steger, Christian; Bittner, Matthias; Jungclaus, Johann; Früh, Barbara; Pankatz, Klaus; Giorgetta, Marco; Reick, Christian; Legutke, Stephanie; Esch, Monika; Gayler, Veronika; Haak, Helmuth; de Vrese, Philipp; Raddatz, Thomas; Mauritsen, Thorsten; von Storch, Jin-Song; Behrens, Jörg; Brovkin, Victor; Claussen, Martin; Crueger, Traute; Fast, Irina; Fiedler, Stephanie; Hagemann, Stefan; Hohenegger, Cathy; Jahns, Thomas; Kloster, Silvia; Kinne, Stefan; Lasslop, Gitta; Kornblueh, Luis; Marotzke, Jochem; Matei, Daniela; Meraner, Katharina; Mikolajewicz, Uwe; Modali, Kameswarrao; Müller, Wolfgang; Nabel, Julia; Notz, Dirk; Peters-von Gehlen, Karsten; Pincus, Robert; Pohlmann, Holger; Pongratz, Julia; Rast, Sebastian; Schmidt, Hauke; Schnur, Reiner; Schulzweida, Uwe; Six, Katharina; Stevens, Bjorn; Voigt, Aiko; Roeckner, Erich (2019). DKRZ MPI-ESM1.2-HR model output prepared for CMIP6 ScenarioMIP ssp585. Version 20211003. Earth System Grid Federation. <https://doi.org/10.22033/ESGF/CMIP6.4403>
- Seferian, Roland (2018). CNRM-CERFACS CNRM-ESM2-1 model output prepared for CMIP6 CMIP historical. Version 20211003. Earth System Grid Federation. <https://doi.org/10.22033/ESGF/CMIP6.4068>
- Smeed, D. A., McCarthy, G. D., Cunningham, S. A., Frajka-Williams, E., Rayner, D., Johns, W. E., ... & Bryden, H. L. (2014). Observed decline of the Atlantic meridional overturning circulation 2004–2012. *Ocean Science*, 10(1), 29-38.
- Song, Zhenya; Qiao, Fangli; Bao, Ying; Shu, Qi; Song, Yajuan; Yang, Xiaodan (2019). FIO-QLNM FIO-ESM2.0 model output prepared for CMIP6 CMIP historical. Version 20211003. Earth System Grid Federation. <https://doi.org/10.22033/ESGF/CMIP6.9199>
- Song, Zhenya; Qiao, Fangli; Bao, Ying; Shu, Qi; Song, Yajuan; Yang, Xiaodan (2019). FIO-QLNM FIO-ESM2.0 model output prepared for CMIP6 ScenarioMIP ssp585. Version 20211003. Earth System Grid Federation. <https://doi.org/10.22033/ESGF/CMIP6.9214>
- Spence, P., Saenko, O. A., Sijp, W., & England, M. (2012). The role of bottom pressure torques on the interior pathways of North Atlantic Deep Water. *Journal of Physical Oceanography*, 42(1), 110-125.
- Steinacher, M., & Joos, F. (2016). Transient Earth system responses to cumulative carbon dioxide emissions: linearities, uncertainties, and probabilities in an observation-constrained model ensemble. *Biogeosciences*, 13(4), 1071-1103.
- Stommel H. 1958 The abyssal circulation. *Deep-Sea Res.* 5, 80–82.
- Stommel, H. (1948). The westward intensification of wind-driven ocean currents. *Eos, Transactions American Geophysical Union*, 29(2), 202-206.

Swart, Neil Cameron; Cole, Jason N.S.; Kharin, Viatcheslav V.; Lazare, Mike; Scinocca, John F.; Gillett, Nathan P.; Anstey, James; Arora, Vivek; Christian, James R.; Jiao, Yanjun; Lee, Warren G.; Majaess, Fouad; Saenko, Oleg A.; Seiler, Christian; Seinen, Clint; Shao, Andrew; Solheim, Larry; von Salzen, Knut; Yang, Duo; Winter, Barbara; Sigmond, Michael (2019). CCCma CanESM5 model output prepared for CMIP6 CMIP historical. Version 20211003. Earth System Grid Federation.

<https://doi.org/10.22033/ESGF/CMIP6.3610>

Swart, Neil Cameron; Cole, Jason N.S.; Kharin, Viatcheslav V.; Lazare, Mike; Scinocca, John F.; Gillett, Nathan P.; Anstey, James; Arora, Vivek; Christian, James R.; Jiao, Yanjun; Lee, Warren G.; Majaess, Fouad; Saenko, Oleg A.; Seiler, Christian; Seinen, Clint; Shao, Andrew; Solheim, Larry; von Salzen, Knut; Yang, Duo; Winter, Barbara; Sigmond, Michael (2019). CCCma CanESM5 model output prepared for CMIP6 ScenarioMIP ssp585. Version 20211003. Earth System Grid Federation.

<https://doi.org/10.22033/ESGF/CMIP6.3696>

Talley, Lynne D. *Descriptive physical oceanography: an introduction*. Academic press, 2011.

Tang, Yongming; Rumbold, Steve; Ellis, Rich; Kelley, Douglas; Mulcahy, Jane; Sellar, Alistair; Walton, Jeremy; Jones, Colin (2019). MOHC UKESM1.0-LL model output prepared for CMIP6 CMIP historical. Version 20211003. Earth System Grid Federation.

<https://doi.org/10.22033/ESGF/CMIP6.6113>

Thomas, M. D., de Boer, A. M., Stevens, D. P., & Johnson, H. L. (2012). Upper ocean manifestations of a reducing meridional overturning circulation. *Geophysical Research Letters*, 39(16).

Voldoire, Aurore (2019). CNRM-CERFACS CNRM-CM6-1-HR model output prepared for CMIP6 CMIP historical. Version 20211003. Earth System Grid Federation.

<https://doi.org/10.22033/ESGF/CMIP6.4067>

Voldoire, Aurore (2019). CNRM-CERFACS CNRM-CM6-1-HR model output prepared for CMIP6 ScenarioMIP ssp585. Version 20211003. Earth System Grid Federation.

<https://doi.org/10.22033/ESGF/CMIP6.4225>

Wang, C., Zhang, L., Lee, S. K., Wu, L., & Mechoso, C. R. (2014). A global perspective on CMIP5 climate model biases. *Nature Climate Change*, 4(3), 201-205.

Weijer, W., Cheng, W., Garuba, O. A., Hu, A., & Nadiga, B. T. (2020). CMIP6 models predict significant 21st century decline of the Atlantic Meridional Overturning Circulation. *Geophysical Research Letters*, 47(12), e2019GL086075.

Wieners, Karl-Hermann; Giorgetta, Marco; Jungclaus, Johann; Reick, Christian; Esch, Monika; Bittner, Matthias; Legutke, Stephanie; Schupfner, Martin; Wachsman, Fabian; Gayler, Veronika; Haak, Helmuth; de Vrese, Philipp; Raddatz, Thomas; Mauritsen, Thorsten; von Storch, Jin-Song; Behrens, Jörg; Brovkin, Victor; Claussen, Martin; Crueger, Traute; Fast, Irina; Fiedler, Stephanie; Hagemann, Stefan; Hohenegger, Cathy; Jahns, Thomas; Kloster, Silvia; Kinne, Stefan; Lasslop, Gitta; Kornblueh, Luis; Marotzke, Jochem; Matei, Daniela; Meraner, Katharina; Mikolajewicz, Uwe; Modali, Kameswarrao; Müller, Wolfgang; Nabel, Julia; Notz, Dirk; Peters-von Gehlen, Karsten; Pincus, Robert; Pohlmann, Holger; Pongratz, Julia; Rast, Sebastian; Schmidt, Hauke; Schnur, Reiner; Schulzweida, Uwe; Six, Katharina; Stevens, Bjorn; Voigt, Aiko; Roeckner, Erich (2019). MPI-M MPI-ESM1.2-LR model output prepared for CMIP6 CMIP historical. Version 20211003. Earth System Grid Federation.

<https://doi.org/10.22033/ESGF/CMIP6.6595>

Wieners, Karl-Hermann; Giorgetta, Marco; Jungclaus, Johann; Reick, Christian; Esch, Monika; Bittner, Matthias; Gayler, Veronika; Haak, Helmuth; de Vrese, Philipp; Raddatz, Thomas; Mauritsen, Thorsten; von Storch, Jin-Song; Behrens, Jörg; Brovkin, Victor; Claussen, Martin; Crueger, Traute; Fast, Irina; Fiedler, Stephanie; Hagemann, Stefan; Hohenegger, Cathy; Jahns, Thomas; Kloster, Silvia; Kinne, Stefan; Lasslop, Gitta; Kornblueh, Luis; Marotzke, Jochem; Matei, Daniela; Meraner, Katharina; Mikolajewicz, Uwe; Modali, Kameswarrao; Müller, Wolfgang; Nabel, Julia; Notz, Dirk; Peters-von Gehlen, Karsten; Pincus, Robert; Pohlmann, Holger; Pongratz, Julia; Rast, Sebastian; Schmidt, Hauke; Schnur, Reiner; Schulzweida, Uwe; Six, Katharina; Stevens, Bjorn; Voigt, Aiko; Roeckner, Erich (2019). MPI-M MPI-ESM1.2-LR model output prepared for CMIP6 ScenarioMIP ssp585. Version 20211003. Earth System Grid Federation.

<https://doi.org/10.22033/ESGF/CMIP6.6705>

Williams, D. N., Balaji, V., Cinquini, L., Denvil, S., Duffy, D., Evans, B., ... & Trenham, C. (2016). A global repository for planet-sized experiments and observations. *Bulletin of the American Meteorological Society*, 97(5), 803-816.

Winton, M., Anderson, W. G., Delworth, T. L., Griffies, S. M., Hurlin, W. J., & Rosati, A. (2014). Has coarse ocean resolution biased simulations of transient climate sensitivity?. *Geophysical Research Letters*, 41(23), 8522-8529.

Wunsch, C. (2002). What is the thermohaline circulation?. *Science*, 298(5596), 1179-1181.

Yan, X., Zhang, R., & Knutson, T. R. (2018). Underestimated AMOC variability and implications for AMV and predictability in CMIP models. *Geophysical Research Letters*, 45(9), 4319-4328.

Yukimoto, Seiji; Koshiro, Tsuyoshi; Kawai, Hideaki; Oshima, Naga; Yoshida, Kohei; Urakawa, Shogo; Tsujino, Hiroyuki; Deushi, Makoto; Tanaka, Taichu; Hosaka, Masahiro; Yoshimura, Hiromasa; Shindo, Eiki; Mizuta, Ryo; Ishii, Masayoshi; Obata, Atsushi; Adachi, Yukimasa (2019). MRI MRI-ESM2.0 model output prepared for CMIP6 CMIP historical. Version 20211003. Earth System Grid Federation. <https://doi.org/10.22033/ESGF/CMIP6.6842>

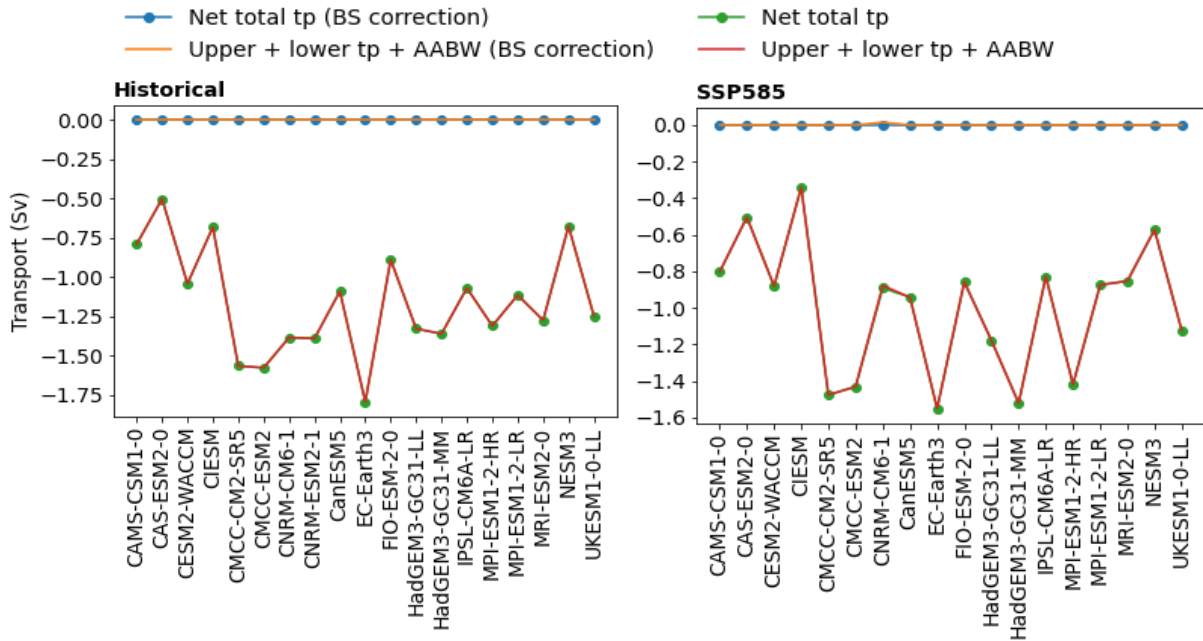
Yukimoto, Seiji; Koshiro, Tsuyoshi; Kawai, Hideaki; Oshima, Naga; Yoshida, Kohei; Urakawa, Shogo; Tsujino, Hiroyuki; Deushi, Makoto; Tanaka, Taichu; Hosaka, Masahiro; Yoshimura, Hiromasa; Shindo, Eiki; Mizuta, Ryo; Ishii, Masayoshi; Obata, Atsushi; Adachi, Yukimasa (2019). MRI MRI-ESM2.0 model output prepared for CMIP6 ScenarioMIP ssp585. Version 20211003. Earth System Grid Federation. <https://doi.org/10.22033/ESGF/CMIP6.6929>

Zhao, J., & Johns, W. (2014). Wind-forced interannual variability of the Atlantic Meridional Overturning Circulation at 26.5 N. *Journal of Geophysical Research: Oceans*, 119(4), 2403-2419.

Appendices

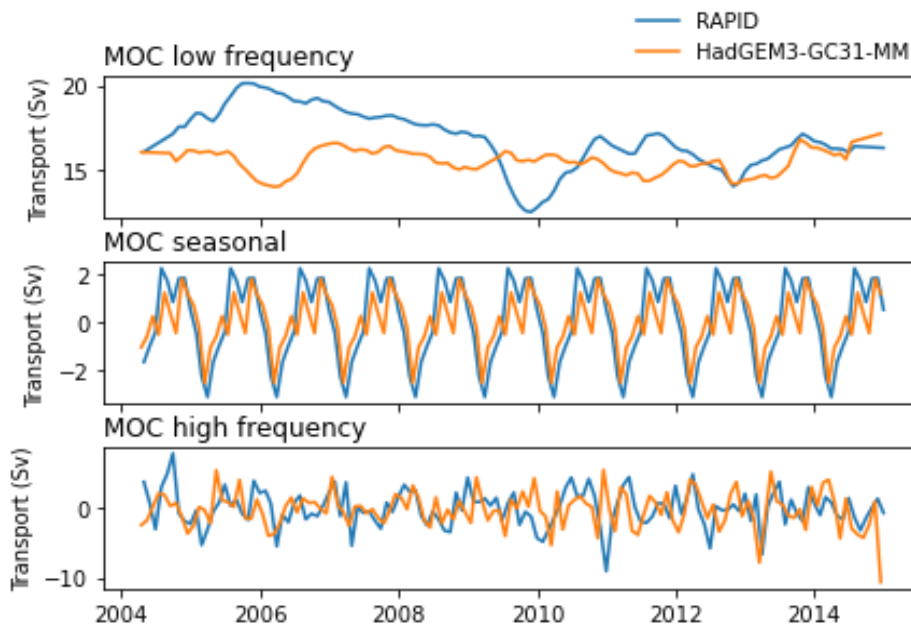
Appendix A

The net transport before and after Bering Strait throughflow correction for historical and ssp585 period. The net transport is based on the sum of the meridional velocity through the cross section and on the sum of all components.



Appendix B

Example of the timeseries of the decomposed variability components. Only the decomposition of the total MOC for HadGEM3-GC31-MM is shown.



Appendix C

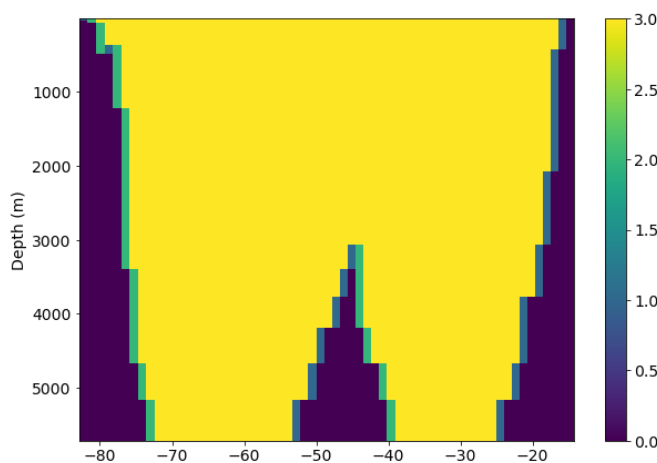
In this Appendix, three examples or method considerations and their effect on transport are shown. These examples include the effect of: (non) removal of halo points, (non) time-varying transport boundaries and the condition that the vertical boundary between FS and mid-ocean transport is located east of the FS maximum.

Halo points

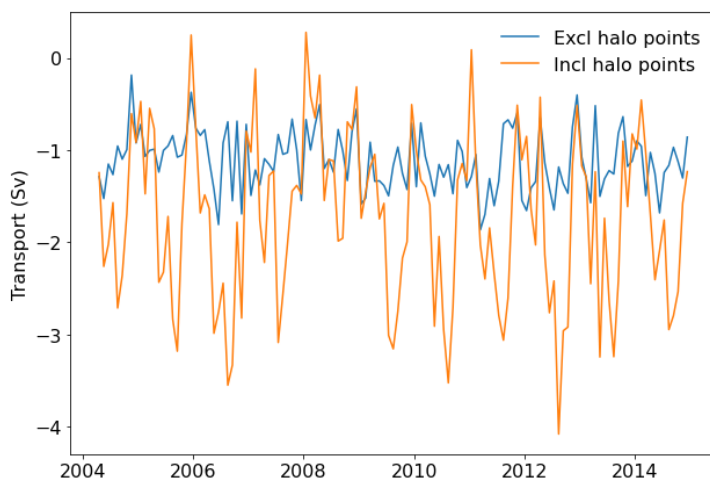
Below, the cross section of MPI-ESM1-2-LR is shown for two masks. For one mask ($mask_{ex}$) the halo points are removed, while for the other mask ($mask_{incl}$) halo points are not removed. Thus $mask_{ex}$ is correct, but we show $mask_{incl}$ to indicate the effect of not removing halo points. The values (y) in the plot are computed by:

$$y = mask_{incl} + 2 * mask_{ex}$$

Since mask values are either 0 or 1, values of y range from 0 to 3. Thus, values of 0 are grid cells that are masked in both masks, values of 1 are grid cells that are only masked by $mask_{ex}$ and values of 2 are grid cells that are only masked by $mask_{incl}$. We observe that $mask_{incl}$ is shifted one grid cell to the east compared to $mask_{ex}$.

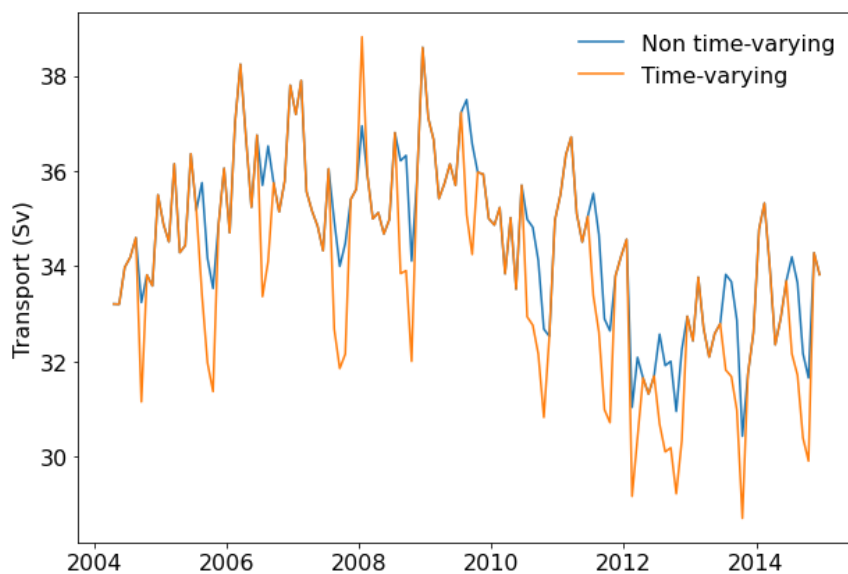


Even though both masks still largely overlap, a significant amount of transport occurs at the western boundary. Therefore, the effect of not removing halo points on the total net transport through the section is extremely large, with almost a factor 3 difference in some years as shown in the plot below. This shows the importance of removing halo points before extracting the data.



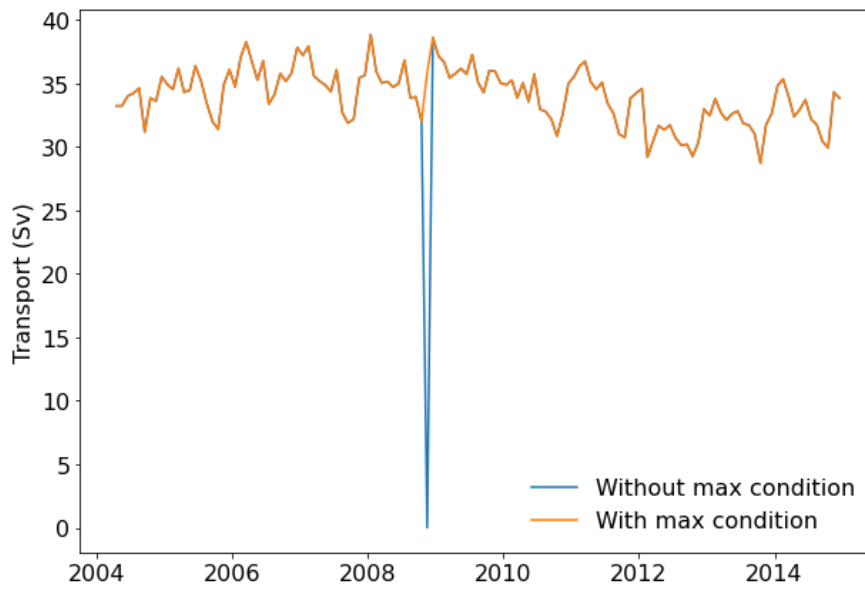
Time-varying boundaries

Below, we show two examples of considerations when obtaining the boundaries between transport components. This has no effect on the net transport through the section, but does influence the strength and variability of the components. In the first example, we observe Florida Straits transport of CAMS-CSM1-0 when boundaries are not allowed to vary in time. In this example, the vertical boundary between Florida Straits transport and upper mid-ocean transport is constant through time, while the depth of maximum overturning varies. Since the depth of maximum overturning is computed by the total zonal transport, the time-varying transport is lower than when the boundaries remain constant for most years. However, this former is the most accurate based on our definition of Florida Straits transport.



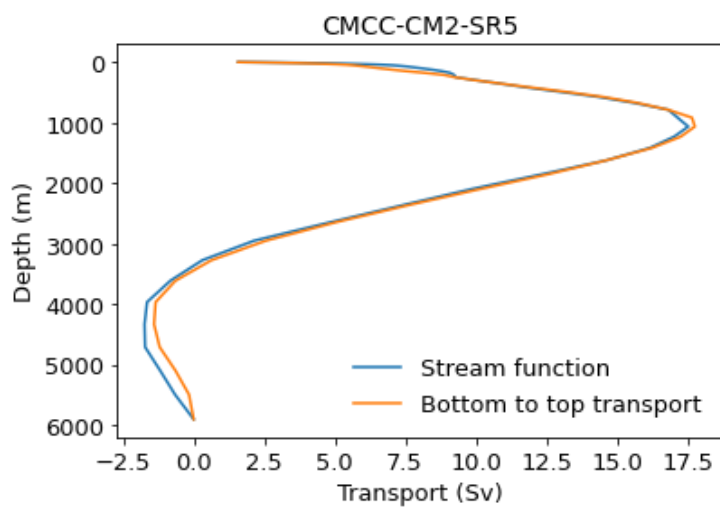
Maximum FS condition

In the second example, we show the timeseries of Florida Straits transport for CAMS-CSM1-0 when the vertical boundary between Florida Straits transport and upper mid-ocean transport is not necessarily east of the Florida Straits maximum. We observe that almost all transport values are the same as when this condition is applied, but the transport of one timestep differs. However, the large deviation does affect the mean strength and variability of Florida Straits transport. Thus, this condition has to be applied when defining the boundaries.



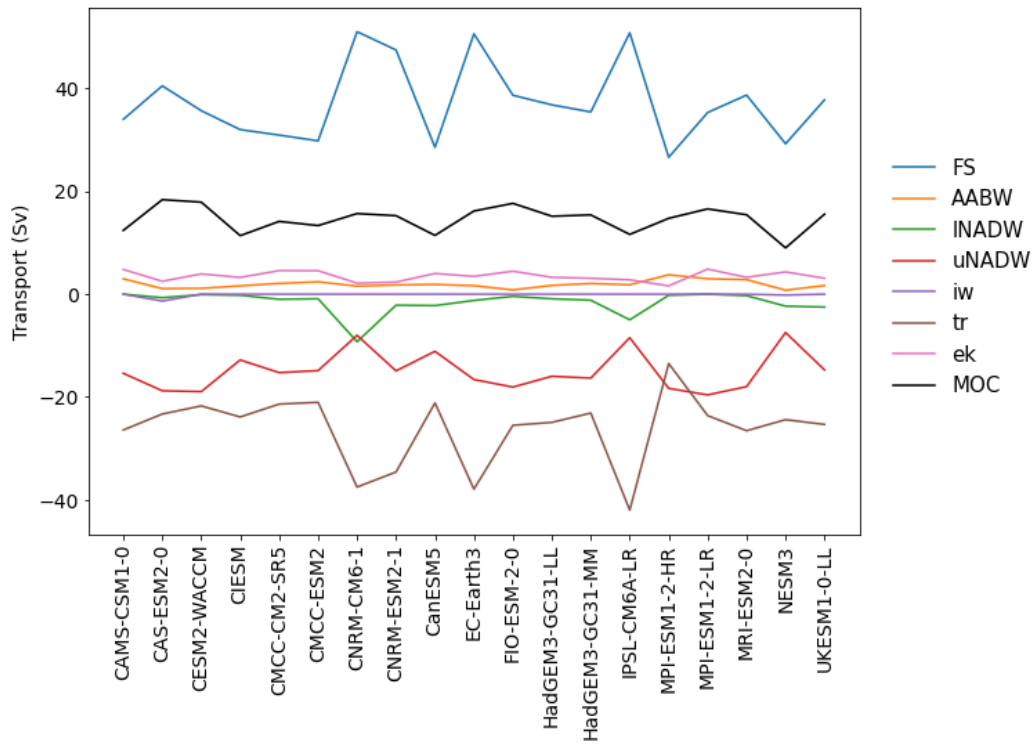
Appendix D

Comparison of the given and calculated overturning stream function for the historical period. Only CMCC-CM2-SR5 is shown as an example.

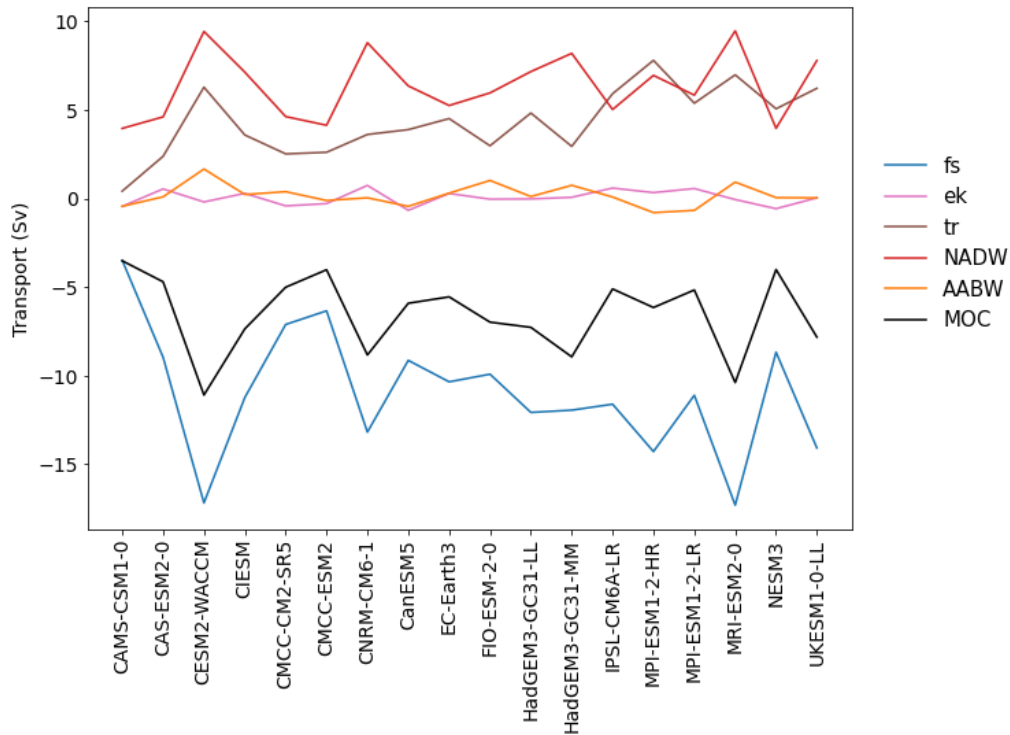


Appendix E

Historical mean of each component for every model. Large inter-model differences are observed.



Future decline under SSP585 of each component for every model. Note that the decline of southward components is positive. Large inter-model differences are observed.



Appendix F

Tables with all correlation coefficients of the variability of the transport components for RAPID data. Bold values are significant within the 95% confidence interval.

Low-frequency

	FS	ek	tr	NADW	AABW	MOC
FS	x	-0.15	0.06	-0.37	-0.23	0.36
ek	-0.15	x	-0.01	-0.35	-0.53	0.40
tr	0.06	-0.01	x	-0.85	-0.67	0.83
NADW	-0.37	-0.35	-0.85	x	0.85	-1.00
AABW	-0.23	-0.53	-0.67	0.85	x	-0.89
MOC	0.36	0.40	0.83	-1.00	-0.89	x

Seasonal

	FS	ek	tr	NADW	AABW	MOC
FS	x	0.17	-0.74	-0.04	-0.18	0.04
ek	0.17	x	0.12	-0.73	-0.72	0.77
tr	-0.74	0.12	x	-0.57	-0.14	0.56
NADW	-0.04	-0.73	-0.57	x	0.61	-1.00
AABW	-0.18	-0.72	-0.14	0.61	x	-0.66
MOC	0.04	0.77	0.56	-1.00	-0.66	x

High-frequency

	FS	ek	tr	NADW	AABW	MOC
FS	x	-0.81	-0.81	-0.81	-0.81	-0.81
ek	0.19	x	-0.81	-0.81	-0.81	-0.81
tr	-0.56	-0.23	x	-0.13	-0.05	0.11
NADW	-0.49	-0.71	-0.13	x	0.77	-1.00
AABW	-0.37	-0.63	-0.05	0.77	x	-0.81
MOC	0.50	0.72	0.11	-1.00	-0.81	x

Tables with all correlation coefficients of the variability of the transport components for CMIP6 data. Bold values are significant within the 95% confidence interval.

Low-frequency

	FS	ek	tr	NADW	AABW	MOC
FS	x	0.10	-0.84	-0.38	-0.18	0.43
ek	0.10	x	-0.10	-0.45	-0.58	0.67
tr	-0.84	-0.10	x	0.05	0.01	-0.09
NADW	-0.38	-0.45	0.05	x	0.12	-0.81
AABW	-0.18	-0.58	0.01	0.12	x	-0.63
MOC	0.43	0.67	-0.09	-0.81	-0.63	x

Seasonal

	FS	ek	tr	NADW	AABW	MOC
FS	x	0.03	-0.70	-0.11	-0.39	0.26
ek	0.03	x	-0.07	-0.55	-0.55	0.69
tr	-0.70	-0.07	x	-0.31	0.15	0.17
NADW	-0.11	-0.55	-0.31	x	0.29	-0.86
AABW	-0.39	-0.55	0.15	0.29	x	-0.70
MOC	0.26	0.69	0.17	-0.86	-0.70	x

High-frequency

	FS	ek	tr	NADW	AABW	MOC
FS	x	0.26	-0.76	-0.29	-0.47	0.47
ek	0.26	x	-0.37	-0.76	-0.67	0.90
tr	-0.76	-0.37	x	0.16	0.31	-0.29
NADW	-0.29	-0.76	0.16	x	0.29	-0.82
AABW	-0.47	-0.67	0.31	0.29	x	-0.77
MOC	0.47	0.90	-0.29	-0.82	-0.77	x

Appendix G

Table with values of the total AMOC for every model. Shown are the historical mean, 2090-2100 mean, absolute change and relative change. Changes are relative to the historical period.

<i>Model name</i>	<i>Historical mean (Sv)</i>	<i>2090-2100 mean (Sv)</i>	<i>Change (Sv)</i>	<i>Change (%)</i>
<i>CAMS-CSM1-0</i>	12.4	8.9	-3.5	-28
<i>CAS-ESM2-0</i>	18.4	13.7	-4.7	-26
<i>CESM2-WACCM</i>	17.9	6.8	-11.1	-62
<i>CIESM</i>	11.4	4	-7.4	-65
<i>CMCC-CM2-SR5</i>	14.2	9.2	-5.0	-35
<i>CMCC-ESM2</i>	13.3	9.3	-4.0	-30
<i>CNRM-CM6-1</i>	15.7	6.9	-8.8	-56
<i>CNRM-ESM2-1</i>	15.3			
<i>CanESM5</i>	11.4	5.5	-5.9	-52
<i>EC-Earth3</i>	16.2	10.7	-5.5	-34
<i>FIO-ESM-2-0</i>	17.7	10.7	-7.0	-39
<i>HadGEM3-GC31-LL</i>	15.2	7.9	-7.3	-48
<i>HadGEM3-GC31-MM</i>	15.4	6.5	-8.9	-58
<i>IPSL-CM6A-LR</i>	11.6	6.5	-5.1	-44
<i>MPI-ESM1-2-HR</i>	14.8	8.6	-6.2	-42
<i>MPI-ESM1-2-LR</i>	16.6	11.4	-5.2	-31
<i>MRI-ESM2-0</i>	15.4	5	-10.4	-67
<i>NESM3</i>	9.0	5	-4.0	-45
<i>UKESM1-0-LL</i>	15.6	7.8	-7.8	-50

Appendix H

Decomposed variability of each component when outlier MPI-ESM1-2-HR is excluded.

